Status report on the WP2 of the

Swiss-Danish instrumentation work packages

for the European Spallation Source, ESS

Εστία

a

focusing reflectometer for small samples

using the

Selene guide concept

Selene
focusing reflectometer

May 15, 2013

Swiss-Danish instrument initiative
ESS
WP 2
reflectometer

Jochen Stahn
Uwe Filges
Panagiotis Korelis
Emmanouela Rantsiou
Tobias Panzner

Ursula Hansen
Marité Cardenas

Paul Scherrer Institut

UNIVERSITY OF COPENHAGEN

project team

Jochen Stahn	Laboratory for Neutron Scattering Paul Scherrer Institut Switzerland `jochen.stahn@psi.ch` +41 56 310 2518	senior scientist - project leader - concept - experiements McStas
Panagiotis Korelis	Laboratory for Neutron Scattering Paul Scherrer Institut Switzerland `panagiotis.korelis@psi.ch` +41 56 310 5813	post-doc - McStas (gravity)
Uwe Filges	Laboratory for Developments and Methods Paul Scherrer Institut Switzerland `uwe.filges@psi.ch` +41 56 310 4606	senior scientist - McStas, MCNPX
Tobias Panzner	Laboratory for Developments and Methods Paul Scherrer Institut Switzerland `tobias.panzner@psi.ch` +41 56 310 4342	pst-doc - McStas - experiements
Emmanouela Rantsiou	Laboratory for Developments and Methods Paul Scherrer Institut Switzerland `emmanouela.rantsiou@psi.ch` +41 56 310 4631	pst-doc - McStas, MCNPX
Marité Cardenas	Nano-Science Center University of Copenhagen `cardenas@nano.ku.dk` +45 35 320 431	senior scientist - scientific advice
Ursula Bengaard Hansen	Nano-Science Center University of Copenhagen `uhansen@fys.ku.dk` +45 60 478 615 (mobile)	student assistant - McStas - experiements
Beate Klösgen	Department for Physics, Chemistry and Pharmacy University of Southern Denmark Denmark `kloesgen@sdu.dk` +45 6550 2561	associate professor - scientific advice

Selene

moon, dark side

titan goddess

detail of the ceiling painting
Selene and Endymion
at the
Ny Carlsberg Glyptotek, Copenhagen

STAP requests after INON3:

1. Instrument layout and dimensions [→2.1] containing details of:
   a. Neutron guide system and beam transport [→2.2][→2.3]
   b. How line of sight is avoided + shielding requirements [→2.4].
   c. Optics and assumptions made define reflectivity for m-coatings etc. [→rest of this document]

2. Choppers: how many, what is the layout and how do they work [→2.5.5]
   a. Detailed Time-distance diagram [→2.5.2]
   b. Used wavelength range(s) [→2.5.1][→2.5.2], bandwidth and resolution as function of λ [→8.3.1]

3. Functional detector specifications determining the required size and resolution [→2.9][→9.2]

4. Feasibility/risks of any new or non-standard components
   [→3] not complete

5. A technical description of how a complete measurements will be performed including
   a. +/- angular range and implications for moving the sample or instrument as this will take time.
   b. How is normalisation of the data performed?
   [→10] not complete
   c. Is measurement during the prompt pulse required, and what is the cost if it is not possible?
   The exclusion of the prompt pulse was requested by the STAP! [→2.5.2][→8.3]

6. What are the tolerances? When does instrument no longer work? (due to e.g. guide quality, if WFM is not possible etc.) [to be done]
   a. This should be demonstrated by simulations, with experimental verification included if available

7. Performance of instrument for standard samples
   We made some simulations using a home-defined sample to start with. [→2.11] From theses we found some *problems* or ambiguities in the sample and parameter definition. As a result we tried to start some discussion at IKON3 and later via e-mail — without any usefull result.

   Our suggestion that one person (preferably at ESS) should do the benchmarking for all concepts (using the subitted instrument files) to ensure a similar interpretation and choice of parameters was rejected.

   Regarding the number of reference samples, various resolutions, possible instrumental errors, and so on, we have no chance to submit the requested simulations anytime soon. Even for the porposal deadline this most likely will not be possible without further man-power (which seems not to be available.)

   We agree that it would be nice to have all these simulations (especially the ones concerning non-perfect conditions), but there is a price for it. In money and in time.
   a. As previously stated this should contain information regarding measurement times for a specified statistical accuracy and is intended to allow the instruments to highlight where they excel as well as where they have weaknesses.
   b. Minimum Reflectivity and how this is achieved for claims below 10-8

8. If applicable, how is beam polarisation and analysis achieved and what is the performance as a function of wavelength. [→2.6]

9. How are off-specular measurements performed and what are the q-ranges and resolution? [→2.10.1]

10. If GISANS is implemented how will this be achieved and what are the q-ranges and resolution [→2.10.4]
    GISANS is not taken into account in detail by now; has to be analysed

11. If SERGIS is implemented what is the intended method? [→2.10.4]
    will be elaborated together with TUM, Germany; method: MIEZE

The points listed in the rest of this document, which are specific to each workpackage, are not comments but points of major concern that the STAP have regarding instrument operation, and that must be addressed, as the STAP feels that there will be a significant performance impact.

SELENE Vertical Sample Reflectometer

The STAP thank the workpackage team for providing a thorough report of the design and test measurement progress. However the concerns previously raised regarding the technical feasibility of the concept have still not been addressed to the satisfaction of the panel.

Major points that require more work:

- issue of frame overlap has not yet been addressed. The position of wavelength band defining and frame overlap choppers need to be added. This must be done in order to assess their impact on the layout of the instrument. [→2.5.4]
  AGAIN: The present instrument design does not contain any choppers. It most likely is no problem to place no chopper wherever you want.

- frame overlap mirrors are to be used instead of a chopper a description of how the divergence of the beam will be managed needs to be included. [→7.1]
  see also previous reports

- precision to which the large focussing mirrors need to be aligned must be assessed and discussed with the ESS in order to assess the practical feasibility of the layout. This is also crucial to understand as settling of the target station during the operational phase will undoubtedly require the realignments of the mirrors. Careful thought should be given to how any problems might be identified and remedied. [→3.1] not complete

- presentation to the whole of IKON highlighted the role of imperfections in the mirrors as a limiting factor in the λ-θ mode. These effects need to be quantified in order to determine if the large mirrors can be manufactured to the required tolerance. [→3.1]

- STAP are still concerned with the contamination of the measured specular signal with off-specular scattering from either the sample or the mirrors and ask that this be quantified. i.e. what percentage of off-specular signal results in a significant deviation of the measured reflectivity curve. [→2.10]
  The *Selene* guide gives a convergent beam which can be used for various measureemnt schemes. One of these involves a slit in front of the sample, resulting in an almost conventional set-up (the beam is still convergent). Whatever is possible on conventional TOF reflectometers is thus also possible on the proposed instrument, including the separation of specular and off-specular signals.

  This separation is also given in the λ-θ encoding mode. Here a possible contamination with the specular scattering off the Bragg peak of the monochromator multilayer might be a challange. But this can be suppressed using a fast moving slit before the sample.

  Only in the high-intensity specular mode the off-specular signal can not be suppressed and forms a (complicated) background. This is the price one has to pay for gaining at least an order of magnitude in counting time. If the off-specular scattering can be neglected, this mode gives a good $R(q_z)$ after data reduction. If not, one can still use this mode to trace the changes in $R(q_z)$ due to external parameters with a high time resolution. If this is not wanted, one should just not use this operation mode!

- work presented from the test measurements at PSI caused concern as the normalisation strategy for the data was unclear and seemed to rely on the use of a supermirror sample. Please clarify the data collection and normalisation procedure. A robust solution to this is essential. [→10.3.6]

- the test experiments done at PSI please quantify the contribution of backgrounds from external sources such as other instruments. This is a concern for the STAP as it was not clear whether the background sources are related to the instrument itself or to its environment within SINQ.
  Most of the background came from neighboring instrueumnts or from BOA / Amor. With each measurement campaign we improved the shielding and thus got a better background situation. The *Selene* intrinsic background is the off-specular scattering from the guide elements. In the meantime additional masks were produced to block the neutrons flying past the guide elements, and the knife blades to block direct line of sight were improved. New results will be available by end of May.

- STAP request that the standard sample simulations are presented using both the angle dispersive (SELENE) mode and the highly compromised (what do you mean by this?) conventional NR mode. i.e. the STAP wish to see the worst case scenario if there are significant problems with the focussing mirrors if there are problems because of off-specular scattering from the mirrors or sample. [to be done]

Εστία — a focusing reflectometer for small samples

The *Swiss-Danish Instrument Initiative* presents Εστία[1], a concept for a focusing reflectometer optimised for small samples. The scientific focus of this instrument is the investigation of the structural and magnetic depth profiles of solid film structures. Probing liquid/solid interfaces or lateral structures is also possible, with a compromised performance. To account for these types of samples we suggest to also build a complementary reflectometer for liquid surfaces and organic samples in general, and eventually one instrument dedicated to the investigation of lateral structures.

The unique feature of Εστία is its truly focusing neutron guide, based on the *Selene* concept. Its point-to-point focusing leads to a drastically reduced beam intensity in the guide, while almost conserving the phase space density actually needed for the measurements. Also the beam is convergent at the sample which avoids over-illumination of the sample (if required) and of the sample environment. The special geometry allows for efficient optics to polarise and filter the beam, or to implement constant resolution without using choppers.

The convergent beam can be used efficiently on sample surfaces reaching from $1 \times 1\,\mathrm{mm}^2$ to $40 \times 10\,\mathrm{mm}^2$. To allow for high detector angles and to reduce the influence of gravity, the preferred scattering plane is horizontal. The wavelength range $\lambda = 5\,\text{Å}$ to $9.4\,\text{Å}$ was obtained by reducing the counting time and avoiding the proton pulse duration for data acquisition.

Εστία provides several operation modes, where switching from one to the other implies only the insertion of some optics or the activation of a slit. In a low-resolution mode it will be possible to investigate dynamic processes in the second time range, or to trace the influence of external conditions on magnetic properties. An other mode gives the performance of a conventional TOF reflectometer, allowing for the separation of specular and off-specular scattering. And using the high divergence of the beam for energy-angle encoding results in a constant resolution for specular reflectivity, a wide q_z-range, and in a *nice* q-space volume for off-specular measurements.

Further options are the generation of a clean parallel beam, e.g. for GISANS experiments, or the addition of spin echo techniques. The instrument will have a full polarisation and polarisation analysis option. It will allow for heavy and bulky sample environment, and accept high magnetic fields.

[1]This is a working title. Estia is the Greek goddess of the hearth, the family, and architecture. In modern Greek the word means *point of interest or importance* and is used for example when adjusting a telescope or a camera lens.

Contents

1 Scientific Case

[5 pages] [Describe the key scientific drivers and relate them to the scientific ambition expected of the ESS. Highlight any new science that the concept would enable and justify its significance in the wider scientific context. Estimate the size and impact of the existing and potential user community. Compare the concept to similar existing instruments and other concepts within the same instrument class at the ESS. Identify the infrastructure and supporting facilities necessary to support the proposed experiments.]

Yet, this is a collection of key-words and ideas — and by far not complete. And it is not fitting the guidelines for the science case chapter!

Typical small samples are hard matter heterostructures where the production process limits the (homogeneous) are to below 1 cm^2. This is e.g. the case for layered metal oxide films grown by pulsed laser deposition (PLD).

...

The need to reach high q_z and thus high detector angles (up to 46° for $q_z = 1\,\mathrm{Å}^{-1}$, 106° for $q_z = 2\,\mathrm{Å}^{-1}$) favours a horizontal scattering geometry. This is also supported by the fact that than gravity affects the beam profile and divergence only in the sample plane.

The only restriction caused by the vertical sample plane is that liquid/gas and liquid/liquid interfaces can not be studied.

1.1 magnetic metallic or oxidic heterostructures

This group of materials are the main target for the small samples reflectometer. Depending on the materials involved the samples are grown by pulsed laser deposition (PLD), sputtering, molecular beam epitaxy (MBE), or the like. Especially PLD-grown samples often suffer from the inhomogeneous thickness of the film for areas larger than $5 \times 5\,\mathrm{mm}^2$. The homogeneity is important not only for the reflectometry measurements, but also it often determines the properties of the film. E.g. the sign of magnetic coupling through a non-magnetic spacer layer might change as a function of the spacers thickness.

example: A widely used substrate for perovskite-type heterostructure is $SrTiO_3$, which upon cooling undergoes several phase transitions. The one at 105 K leads to a twinning and as a consequence to a fragmentation of the surface, where the individual facets reflect in different directions. With a small footprint one can reduce the number of active facets for measurements.

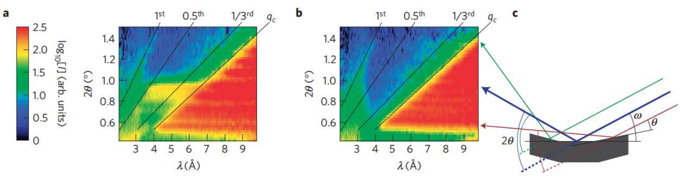

Reflectivity measured on a curved sample surface with a highly collimated incoming beam. The individual facets of the surface correspond to the steaks with $\theta =$ const.. [?]

compatibility Samples investigated with synchrotron radiation methods often are below $1\,\mathrm{cm}^2$ to fit in the HV sample environment. The presented instrument would be able to investigate the same samples for complementary information. E.g. in combination with XRD, XMCD and resonant x-ray reflectometry. Other probes like SQUID impose an even stronger restriction by accepting $5 \times 5\,\mathrm{mm}^2$, only.

contacts Samples showing eclectic effects (polarisation, multiferroic properties) often need to be conducted. A focused beam then allows to measure in a region without contacts to avoid uncontrolled absorption, background and eventually phase shifts in part of the reflected neutrons (e.g. contact/film interface instead of vacuum/film).

example An other challenge with electronic devices is that a single point defect in an isolating layer might lead to the failure of the device. Possible solutions are a patterning followed by the selection of good contacts, or the reduction of sample size.[1]

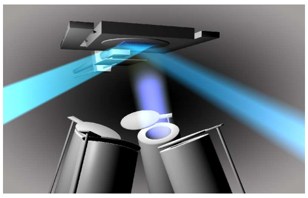

1.2 non-magnetic metallic or oxidic heterostructures

1.3 soft matter films and heterostructures on a substrate

Since samples of this type often can be produced with surface area of $10\,\mathrm{cm}^2$ to $100\,\mathrm{cm}^2$ they would profit from a footprint width larger than $\approx 1\,\mathrm{cm}$. Nevertheless they can be investigated on this instrument.

... rare substances ....

... expensive material ....

1.4 liquid/solid interfaces

Liquid/solid cells can be mounted and measured without problem. Since the footprint can be defined exactly far before the sample it is possible to avoid the illumination of the gasket and the liquid vessel. Again, for larger cells the width of the footprint might be less than acceptable by the sample. On the other side one can even reduce the footprint to scan the interface for inhomogeneities (e.g. non-perfect coating or air bubbles).

1.5 laterally structured surfaces

For these it is essential to measure the off-specular reflected signal. This is possible by using a slit directly after the guide (2.4 m or 4.5 m form the sample) which leads to an almost conventional TOF reflectometry set-up. "Almost" means that the beam is still convergent! The slit just defines the θ-range, not the footprint size. Moving the slit between pulses allows to vary θ without rocking the sample.

1.6 non-perfect surfaces

1.7 GISANS

1.8 spin-echo techniques

In cooperation with Robert Georgii and Wolfgang Häußler, both from the Technical University Munich, we investigate the possibility to have a MIEZE set-up as an add-on. The second coil could be installed in the space before the sample, the first one in an equivalent position before the a guide element. This way all trajectories between the coils are of the same length. (→ **??**)

The space before and behind the sample would also allow for the installation of a SERGIS set-up.

2 Description of Instrument Concept and Performance

[10 pages] [Describe the instrument concept and evaluate its expected performance using relevant performance indicators (as defined for the instrument class by the corresponding STAP). Explain how the concept addresses the scientific drivers described above. Justify how the concept makes use of the ESS long-pulse structure.]

It is proposed to build a polarising reflectometer, optimised for samples of 1 cm^2 area, or less, capable to cover a wide q_z range with variable resolution. The scattering plane is horizontal to allow for wide detector angles. The unique feature of this instrument is its truly focusing guide system, which reduces background and illumination of sample environment, and which opens new possibilities for beam shaping and filtering.

In the following the lay-out of the instrument is presented, followed by a presentation of the guide system and its key features. These strongly influence the design of the components presented thereafter. The essential parameters of the instrument are given in table 2.1.

The final sections of this chapter deal with the operation schemes [→2.10], simulations [→2.11], and a discussion of the performance [→2.12].

Table 2.1: Key features of the reflectometer for small samples.

parameter space		
q_z-range	$[0, 1]\,\mathrm{Å}^{-1}$	to be covered in 5 measurements
λ-range	$[5, 9.4]\,\mathrm{Å}$	
sample size	$[0.3, 40] \times [0.3, 10]\,\mathrm{mm}^2$	$x \times y$
maximum divergence	$\Delta\theta_{xy} = 1.5°$	scattering plane
	$\Delta\theta_{xz} = 1.5°$	sample plane
resolution		
intrinsic $\Delta\lambda/\lambda$	2.1%	5.0 Å
	4.0%	9.4 Å
$\Delta q/q =$ constant	3%, 5%, 10%, ...	with multilayer monochromator
geometry		
scattering plane	horizontal	
total length	58.0 m	
sample / detector	6.2 m	
2θ	$-2°$ to $50°$ $(110°)$	for $q_z \leq 1\,\mathrm{Å}^{-1}$ $(2\,\mathrm{Å}^{-1})$
moderator	cold	
guide transmission	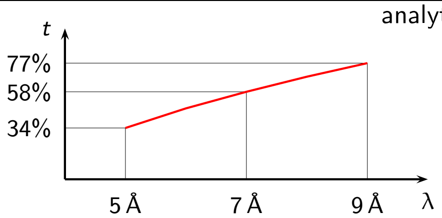	analytical, based on eqn. 6.5.2
λ t		
5 Å 34%		
6 Å 47%		
7 Å 58%		
8 Å 68%		
9 Å 77%		

2.1 instrument lay-out

The principle instrument lay-out is shown in figure 2.1. The various components are briefly presented here. A more detailed discussion follows in the next sections.

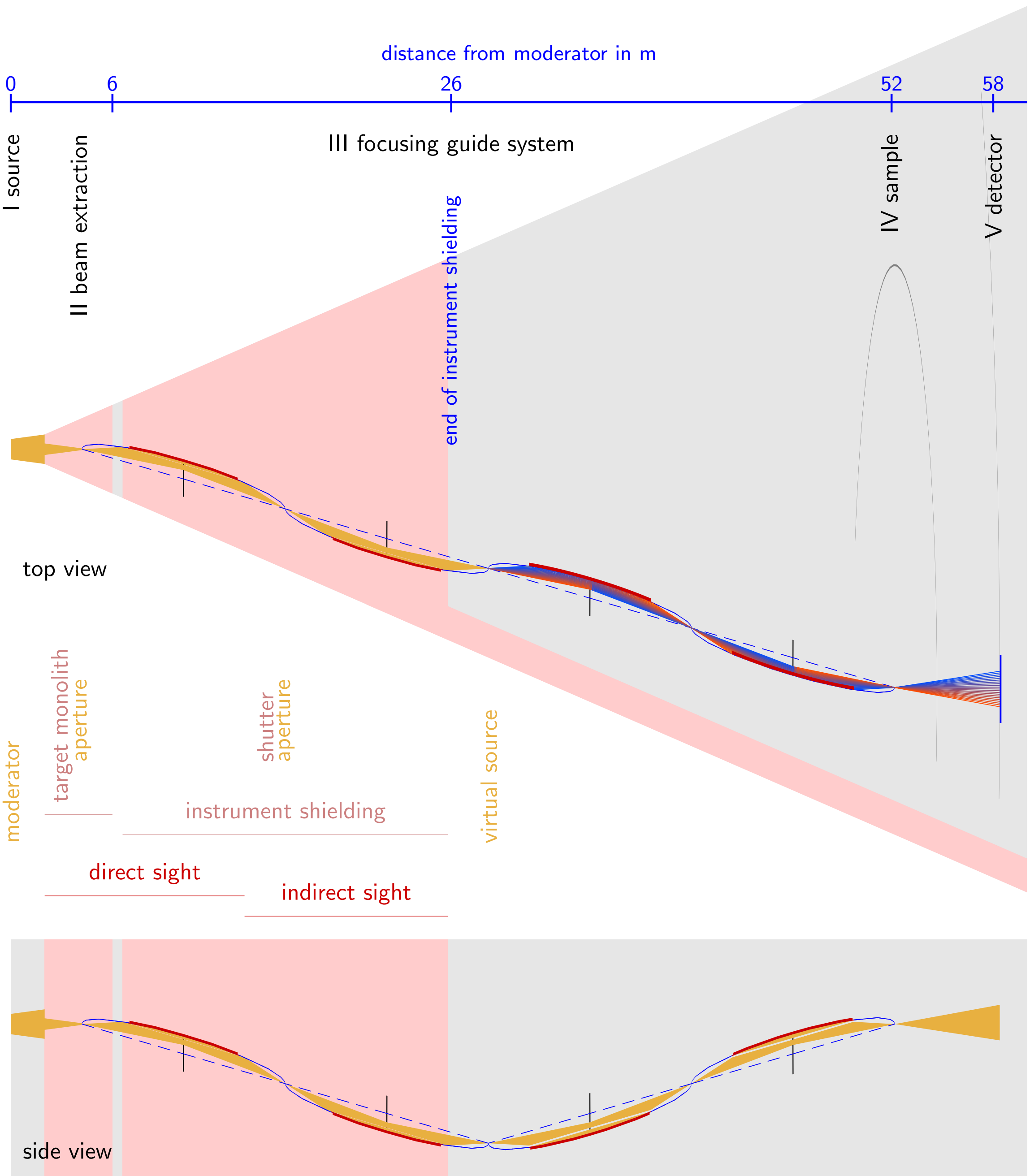

Figure 2.1: Sketch of the instrument lay-out. The direction normal to the beam is stretched by a factor 10 for clarity. The gray area in the upper sketch represents a 5° wedge on the floor. The detector will move outside this area for high angles. The light red area represent shielding, i.e the target monolith, the common instrument shielding and individual instrument shielding. The thick red lines represent the *Selene* guide segments, where the blue lines give the shapes and the long axis of the related ellipses. The golden area are the beam paths within the extraction unit and the first *Selene* guide section. For the second section the λ-θ encoding mode is shown, where the λ is here encoded in a colour reaching from red to blue. (For the nomenclature of the components, please refer to table 5.1.)

I source The instrument needs a cold moderator as neutron source, where the effective flux maximum (i.e. including losses and rescaling [→2.5.1]) determines the minimum wavelength $\lambda_{\min}$.

II beam extraction [→2.3] The purposes of the beam extraction unit are to form a pin-hole at $x = 4.2$ m of $10 \times 10\,\mathrm{mm}^2$, and otherwise to stop as many fast neutrons and γ radiation as possible.

III focusing guide system [→2.2] The essential difference of the presented instrument compared to conventional reflectometers is the truly focusing guide system.

Between the pin-hole forming a virtual source, and the sample a focusing guide system is realised, based on the *Selene* concept. The complete guide consists of 4 segments, each a 7.2 m long elliptically shaped reflector where the focal point distance is 12 m. The usage of 4 instead of 2 longer segments allows to get out of line of sight twice at $x \approx 25$ m, and to use the mentioned pin-hole in the extraction unit.

The first 2 segments create an image of the pin-hole in the mid of the guide ($x = 28.2$ m, in the following referred to as *virtual source*), where precision beam-shaping and λ- and polarisation filtering is then performed. The last 2 segments focus the clean beam to the sample.

Additional beam-defining elements like slits, choppers, polarisers, and monochromators, can be located in the spaces at $x \in [25.8, 30.6]$ m, $x \in [25.8, 42.6]$ m, and $x \in [49.8, 52.2]$ m.

IV sample [→2.7] The sample is located at the final focal point at $x = 52.2$ m. The *Selene* guide ends 2.4 m upstream the sample position. This and the focused beam (making a nearby slit obsolete) allow for installing voluminous sample environment.

V detector [→2.9] A position sensitive detector is located at $x = 58$ m, where its angular resolution dominates the resolution of this instrument concept. For diffraction a second, shorter detector arm allowing for higher 2θ can be installed.

2.2 Selene guide

task: deliver a focused beam to the sample with adjustable divergence and footprint

Since the *Selene* guide dominates the complete instrument lay out, it is presented first. Special aspects discussed in the appendix are: design considerations [→6.1], coma aberration [→6.3], and chromatic aberration due to gravity [→6.4].

The reason for using a truly focusing guide is that it allows for shaping the phase space required at the sample already at the guide entrance. This has the consequences that radiation issues and illumination of the sample environment are strongly reduced. It is important to notice that most other guide concepts based on elliptic guides are not exactly focusing: They suffer from strong coma aberration effects and create a divergent beam at the exit. [2]

The *Selene* guide can be seen as an extended Montel optic as used at synchrotron beam-lines. Two planar-elliptic reflectors form a gorge with L-shaped cross section. The distance of the guide entrance to the virtual source at the initial focal point is chosen in a way to avoid multiple reflections for each reflector. The first

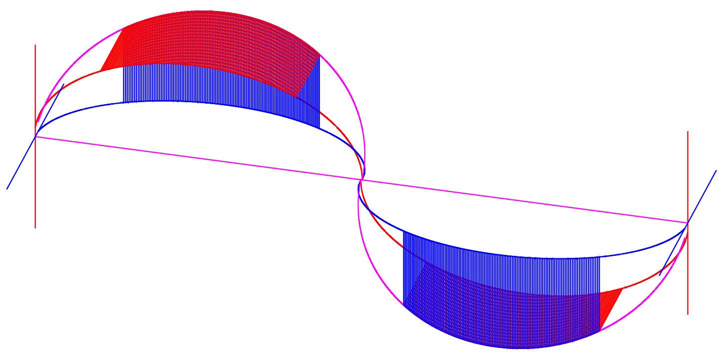

Figure 2.2: Sketch to illustrate the shape of the *Selene* guide. Shown are two segments with L-shaped cross section, sharing the long axis (magenta) and a focal point.

Table 2.2: Parameters of the *Selene*-type guide. For a given instrument length of 58 m and $\Delta\theta_{xy} = \Delta\theta_{xz} = 1.5°$ the following guide parameters are obtained by analytical calculations. [→6.1]

guide parameters		
c	6.0 m	half distance between focal points
ξ	0.6	effective length of the build guide
b/a	0.01754	$\Rightarrow$ $b = 105.26$ mm, $a = 6000.92$ mm
distances		
moderator / pin hole	4.2 m	first focal point
$2c$	12.0 m	length of ellipses
$\xi \cdot 2c$	7.2 m	length of (coated) guide sections
$(1-\xi)\cdot 2c$	4.8 m	space between guides
$(1-\xi)\cdot c$	2.4 m	space before sample
sample / detector	[1.5 . . . 7.5] m	high-angle diffraction vs. high resolution
Δz at sample	0 / 522.7 mm	vertical offset of one *Selene* section
Δy at sample	0 / 522.7 mm	horizontal offset of one *Selene* section
free space withing flight-path for beam- / pulse-shaping (distance from the moderator)		
$x =$ 6.0 m → 6.6 m		gap behind target monolith
13.8 m → 18.6 m		eventually frame-overlap chopper
25.8 m → 30.6 m		precise beam-shaping, polarisation
37.8 m → 42.6 m		
49.8 m → 52.2 m		before sample
coating		
m	3.0	critical edge
coated area	4 m^2	
material	Ni/Tisupermirror	

guide segment creates an image at its second focal point which is blurred due to coma aberration. To correct for this, an identical guide segment is used, mounted parallel to the first one, but reflecting in the opposite direction. This inverts the coma effect and re-establishes the image of the virtual source at the final focal point. A sketch of the guide geometry is shown in figure 2.2

The guide system for the presented reflectometer consist of two such *Selene* guide sections: The first has to create a virtual source with defined size and divergence, but twice out of line-of-sight from the moderator. This virtual source is in a low-radiation region so that sensitive mechanical equipment and optics can be used there. It is also possible to access this area for maintenance during operation (with the instrument shutter closed). At and around the virtual source point the beam is shaped according to the needs on the sample. The shape and orientation of the footprint of the beam on the sample can be defined by an adequate slit system. The second *Selene* guide has to map the shaped beam to the sample. The divergence (and eventually the incident angle) of the beam are defined by slits before or after the guide segments. This way spot-size and divergence are adjusted independently.

The use of two *Selene* guides has the consequence that each neutron is reflected exactly 8 times before it arrives at the sample. The resulting reduction in intensity is the price one has to pay for low radiation and convenient beam manipulation. [→2.5.1]

Table 2.2 gives the geometrical parameters of the ellipses, the measures of the guide and the coating.

2.3 beam extraction

task: transport the requested phase space volume outside the target monolith, while reducing the radiation as much as possible

Within the first 6 m the only *optics* needed is a pin-hole at $x = 4.2$ m acting as a virtual source for the first *Selene* guide section. The location is chosen to accept the required divergence of $\Delta\theta = 1.5°$ from the 120×120 mm^2 wide moderator. The extraction insert consists of some highly γ and neutron absorbing material (e.g. copper).

There is no restriction for including a maintenance shutter in the monolith or in the extraction insert at any position.

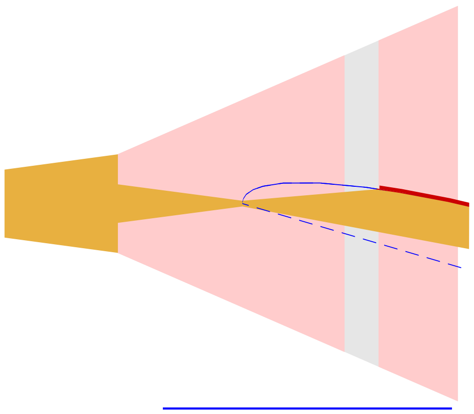

Figure 2.3: Sketch of the beam extraction section with a pin hole. A small ($10 \times 10\,\mathrm{mm}^2$) aperture 4.2 m from the source acts as virtual source and defines the initial focal point for the first *Selene* guide section. This position allows for a divergence of $\Delta\theta_{xy} = \Delta\theta_{xz} = 1.5°$. The openings of the flight path section are 68 mm / 58 mm at the entrance / exit of the target monolith.

2.4 shielding

It is inherent to the *Selene* guide concept that neutrons are reflected on each reflector once, so that a shielding behind the first guide segment can stop all transmitted neutrons. An absorber opposing the centre of the reflector blocks all direct trajectories from the pin-hole to a space behind the first guide segment. The second guide segment repeats this scheme so that at the end of the shielding around and behind the first *Selene* guide the view to the moderator is blocked twice, as is required by the ESS [→8.2]. There is space for a vacuum housing and mounting equipment around the guide. The guides open construction (it forms an L, rather than a rectangle) allows for a tight shielding on two sides, the support mechanics can be mounted on the other sides.

Figure 2.4 shows the shielding concept for the first *Selene* guide section including the target monolith. Behind the monolith there is a gap of 600 mm until the first guide starts. Unless used for filters or a shutter, this gap can be filled by an extension of the insert.

The first and second guide elements ares enclosed in a heavy concrete block. In the sketch at least 50 mm free space between guide and shielding are assumed for support, alignment devices, and vacuum housing. Because the dimensions of the openings are about 3 times the actual guide width, additional shielding is needed before and after the concrete shielding. These masks are supposed to consist of copper (displayed in blue). The area directly irradiated from target and moderator ends at the exit of the first concrete block at $x = 13\,800$ mm. The indirectly irradiated area ends at $x = 25\,800$ mm, i.e. less than half way between source and detector. In the gap $x \in [14, 18]$ m optical elements, the instrument shutter and eventually a frame overlap chopper can be installed, again surrounded by a concrete shielding.

The support system for the guides needs more space than just the $160 \times 160\,\mathrm{mm}^2$ within the channel. Swiss-Neutronics suggested to use a granite beam to support the guide. This could also be part of the shielding, with appropriate shape to prevent straight holes parallel to the channel. If granite is suited for this purpose has to be investigated. On the other side one could use a heavy concrete beam as support, if it is stable enough also against thermal influences.

The second *Selene* guide section will need some shielding, too, but since neither thermal or fast neutrons, nor γ-radiation should reach this region, only a moderate boron-based absorber should be sufficient. To ensure the absence of fast neutrons, a sapphire filter can be inserted behind the concrete shielding.

2.4.1 MCNPX simulations

!!! Based on the model given in figure 2.4 MCNPX simulations have been performed by U. Filges, PSI. The results are summarised in table 2.3. For these simulations it was assumed that the space between the shielding is *evacuated*, i.e. air-scattering is not included.

These results tell that the proposed geometry and dimension of the *Selene* guide allows for a shielding which fulfils the requirements by the ESS. A more realistic model with a floor, additional shielding around the (now open) beam path, a higher target monolith, guides and air is planned.

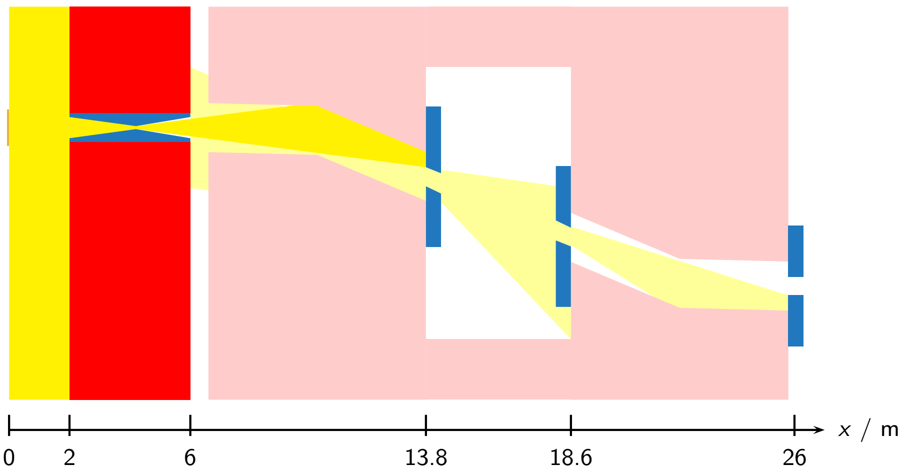

Figure 2.4: Sketch of the fast neutron and γ shielding concept. Here a vertical cut through the shielding is shown, following the beam in horizontal direction. The guide geometry and thus the shielding is the same horizontally and vertically. The source (moderator) is represented by the brown rectangle on the left. The red area stands for the monolith, the blue insert is the extraction unit. The pale red area represent heavy concrete shielding (or a sandwich of various moderators and absorbers), which hosts the guide elements. Additional masks (here blue) are needed to block the opening outside the neutron beam path. The area directly illuminated from the source is shaded yellow, the indirectly illuminated area is pale yellow. The neutron guides are not shown.

x position	y/z position	dose rate / µSv γ	dose rate / µSv neutron
exit monolith	in beam	$8 \cdot 10^3$	$5 \cdot 10^8$
exit common shielding	in beam	$5 \cdot 10^2$	$6 \cdot 10^4$
	off beam	–	$1 \cdot 10^4$
entry instrument shielding		$8 \cdot 10^{-1}$	$5 \cdot 10^2$
exit instrument shielding	in beam	–	–
	off beam	–	–
5 m behind shielding	in beam	–	–

Table 2.3: Dose rates calculated with MCNPX for various positions along the guide. The computational statistics was too low for the positions marked with –.

new numbers !!!

2.4.2 shutter

An instrument shutter can be placed in the gap between the first and the second guide segments. This region is already out of line of sight from the moderator, so that only secondary radiation and cold neutrons transported by the guide have to be blocked.

2.5 energy- and time range

The time and energy characteristics of the ESS long-pulse source allows for a relatively wide λ range, while keeping the intrinsic instrument resolution below $\approx 4\%$, and avoiding the proton pulse time for measurements. A full reflectivity curve is thus achieved by piecing together (a few) measurements with varying ω, only. Further stitching due to complex chopped beam characteristics is not necessary.

2.5.1 flux and $\lambda_{\rm min}$

The experience with existing TOF reflectometers is, that the lower limit of the wavelength spectrum $\lambda_{\rm min}$ corresponds to the effective flux maximum at the sample position. The reason is that even smaller λ result in higher q_z and thus in general in lower reflectivity, and at the same time in a lower incident intensity. Thus

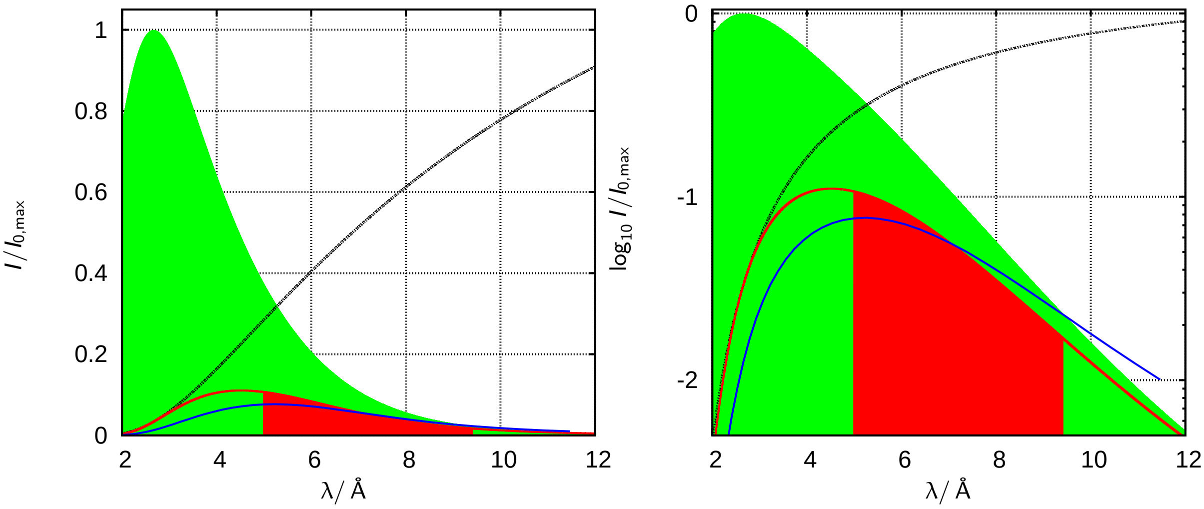

Figure 2.5: Spectra $I(\lambda)/I_0$ (left) and $\log_{10} I(\lambda)/I_0$ (right) as given by the source (green area), after attenuation according to eqn. (6.5.2) with 8 reflections (red line), and after re-binning it to $\Delta\lambda/\lambda = 2\,\%$ (blue line). The latter line is scaled by an arbitrary value. The black line is the transmission of the guide. The source spectrum $I_0(\lambda)$ is the one used by the McStas component `ESS_moderator_long`. The red area represents the neutrons actually arriving at the sample.

the accuracy of the data rapidly decreases and it is much more appropriate to measure at a higher angle of incidence to access the corresponding q_z range.[1]

The effective flux at the sample can be estimated by reducing the initial flux $I_0(\lambda)$ by the losses due to reflections on the guide walls, and by taking into account that in the end one aims for $\Delta q/q =$ constant or something quite close.

The double *Selene* guide concept involves 8 reflections for all neutrons on surfaces with a non-perfect reflectivity R. Since the angle of incidence on the guide surface hardly varies along the guide for the presented concept, one can assume an attenuation of [→6.5] $I(\lambda) \approx I_0(\lambda) \cdot R(\lambda)^8$.

A more prominent effect has the required $\Delta q/q =$ constant: effectively the time-bins, and thus the λ-bins necessary for $R(q_z)$ curves follow $\Delta\lambda/\lambda =$ const which shifts the spectral wight to the bins with large λ. This shift can be approximated by $I(\lambda)_{\Delta\lambda/\lambda=\text{const}} \propto \lambda \cdot I(\lambda)_{\Delta\lambda=\text{const}}$

This way the minimum wavelength $\lambda_{\min} = 5$ Å was determined as illustrated in figure 2.5.

2.5.2 time regime and $\lambda_{\max}$

In order to avoid a contamination of the measurement with background originating from the proton pulse and secondary processes, the instruments length was chosen so that the 5 Å neutrons arrive at the detector right after a pulse. This leads to a minimum length (moderator to detector) of 58 m. And the time between pulses sets the upper wavelength limit to $\lambda_{\max} = 9.4$ Å. Figure 2.6 shows the corresponding t-x-diagram.

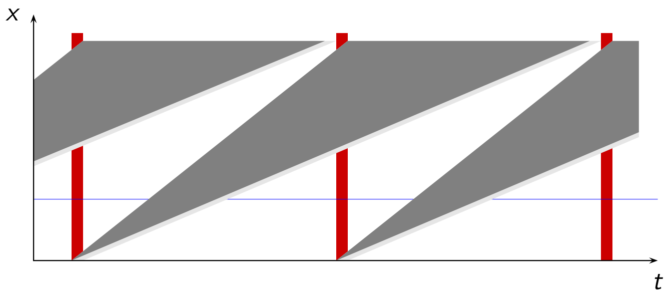

Figure 2.6: Sketch to illustrate how to avoid the influence of the γ and fast neutron burst from the proton pulse hitting the target. The sketch is to scale with period $T = 70$ ms, pulse length $t = 3$ ms, and a sample detector distance of 58 m, i.e. $\lambda \in [5, 9.4]$ Å.

[1] In case the width of the q_z-range covered within one pulse is essential, one might accept also a smaller $\lambda_{\min}$ for the cost of a dramatically increased measurement time.

2.5.3 intrinsic λ resolution

The time- and thus the λ-resolution is $\Delta\lambda \approx 0.2$ Å, given by $\lambda \in [5, 9.4]$ Å, the moderator-detector distance of $X = 58$ m, and the pulse length τ. [→8.3.1] This leads to $\Delta\lambda/\lambda = 2.1\%$ at $\lambda = 9.4$ Å, and $\Delta\lambda/\lambda = 4.0\%$ at $\lambda = 5.0$ Å.

2.5.4 frame-overlap suppression

For neutrons with $\lambda < \lambda_{\mathrm{min}} = 5$ Å the coating of the guide acts as a filter. If necessary a Be-filter can be used to further suppress the range $\lambda < 4$ Å.

Neutrons with $\lambda > \lambda_{\mathrm{max}} = 9.4$ Å will be suppressed by using a transmission filter. A silicon wafer with a Ni coating ($m = 1$) shaped like a logarithmic spiral [→7.1] is installed before the virtual source. The shape assures that all trajectories pointing towards the virtual source hit the wafer at the same angle (here 0.95°).

2.5.5 choppers

For this instrument and the operation schemes presented in section 2.10 no choppers are foreseen.

In case the frame-overlap suppression as described in 2.5.4 proves to be insufficient, it is possible to add a frame-overlap chopper later on close to the focal point at $x = 16.2$ m (blue line in figure 2.6). There the beam cross section is of the order $30 \times 30\,\mathrm{mm}^2$. This leads to relaxed specifications for the chopper. Neglecting opening times for a first approximation the chopper should be open for $t \in [0.020, 0.040]$ s (for $\lambda \in [5, 9.4]$ Å). The next higher order is transmitted for $t \in [0.090, 0.110]$ s and corresponds to $\lambda \in [22, 27]$ Å.

For the moment, no chopper is foreseen there and the λ filtering is meant to be realised with a reflecting mirror [→7.1].

Since the *Selene* guide system in the end fulfils the same task as a *normal* guide, it can be combined with multi-chopper setups for Repetition Rate Multiplication or for Wavelength Frame Multiplication [3]. In the large free regions between the guide segments of the *Selene* guide this would not cause any modifications to the guide. A chopper within the reflecting part results in gap in the divergence distribution.

2.6 polarisation

Neutron spin polarisation and its analysis are key-features of the reflectometer for small samples. Based on the demands nowadays one can estimate at least 50% of the measurements will need a polarised beam, and at least 10% also polarisation analysis.

The concepts presented below are either well established, or under development so that there is no unknown risk connected. Besides to permanent coating, the options can be altered later on.

2.6.1 permanent polarisation

A permanent polarisation can be achieved using an appropriate coating on (one side of) one guide segment. This has the advantages that off-specular scattering from the coating will not hit the sample, and that the distance from a high magnetic field at the sample position is sufficiently large to prevent depolarisation.

2.6.2 optional polarisation

In case the 50% loss due to polarisation is not accepted, there are several approaches possible:

polarising (double bounce) reflector The ML monochromator used for λ-θ encoding or any reflector close to the initial focal point can have a polarising coating.

polarising filter By using a transmission filter with the shape of a logarithmic spiral as discussed in section 7.1 it is possible to polarise a divergent beam emerging form a small source with a moderate m of the SM coating (and thus a high polarisation efficiency).

E.g. a combined λ low-pass and polariser for $\lambda \in [5, 10]$ Å, $\Delta\theta = 1.5°$, and a distance of the polariser from the focal point of 300 mm leads to a device of ≈ 1 m length. The polarising coating has $m = 2$.

^{3}He polariser The small beam size close to the initial (intermediate) focal point allows for the operation of a rather small ^{3}He cell. Typically with a cross section of a few cm^2, only. In addition, the long distance from this point to the sample avoids depolarisation due to high magnetic fields, there.

2.6.3 analyser

The different beam geometry behind the sample demands for more complex and larger devices.

analysing filter This is the analogue to the polarising filter, but it is not realistic to install it some 300 mm behind the sample. Thus a larger multi-channel device directly in front of the detector has to be build. This is a new concept and has not been tested, yet.

wide-angle analyser based on supermirrors A SM-based multi-channel bender can be installed directly in front of the detector. Similar devices are in operation at FOCUS@PSI and at HYSPEC@SNS.

^{3}He analyser The wide divergence and the needed distance from the sample (to avoid the influence of the sample magnetic field) mean that a large ^{3}He is needed.

2.6.4 flipper

RF flipper The divergent polychromatic beam can be flipped by using a RF flipper.

RSF flipper An alternative approach for monochromatic beams changing the wavelength with time is a Resonance Spin Flipper [4].

switchable rem anent coating For the devices based on SM coatings for polarisation / analysis one can use magnetically remanent coatings, allowing for flipping the polariser, rather than the beam.[5]

2.7 sample stage

The sample stage is the same as for conventional reflectometers. It either uses a hexapod or a classical tower of translation- rotation-, and tilting-stages.

The position of the stage on the floor might vary with the alignment and the operation mode of the instrument. I.e. a *x*-*y* translation stage (or a platform on air-pads) forms the basis.

Since the sample environment can be quite heavy and voluminous, the sample stage should be able to handle wights of up to 1 t. The *free* space between the platform and the sample should be at least of the order of 300 mm. In table 9.1 a possible set-up of translation and rotation devices is listed. The complete sample stage should be non-magnetic, because one principle application of this instrument will be the measurements in high magnetic fields.

The guide ending 2.4 m before the sample leaves enough space for a fast slit system [→2.8.3] and even large sample environmental devices like troughs or cryomagnets. Also an equipment for complementary measurements like UV, or X-ray will find space.

2.8 beam shaping

2.8.1 beam definition

The beam shape at the sample position is essentially defined in between the two *Selene* guide sections, 24 m upstream. The symmetry of the problem tells that the same degree of freedom will be needed there as at the sample stage [→2.7], but with a much reduced demand concerning load.

Since the focal point position does only change due to misalignment of the first *Selene* guide section, the base-*x*-*y* translation needs to cover only a small area, only.

2.8.2 apertures within guides

To block the direct line of sight through the *Selene* guide and to reduce the divergence, one-sided apertures are positioned close to the centres of the 2^{nd} guide segment for both guide sections. The one in the first guide is rather heavy, but does not need to be very accurate, since it should just reduce the radiation level outside the shielding. The apertures in the second guide will be used for precise beam divergence definition and thus need to be very accurate. On the other side, the blades are much thinner and thus lighter.

2.8.3 fast aperture

Behind the *Selene* guides, some 2.2 m before the sample a precise and fast slit system might be used optionally. For the conventional operation mode it defines the angle of incidence and the divergence. *Fast* here means that position and opening of the slit can be varied between pulses within 10 ms.

If technically possible it could also be used in the λ-θ encoding mode, to cut down the unwanted off-specular intensity from the monochromator by scanning the slit across the beam during one pulse.

2.9 detector

2.9.1 area detector

For the reflectometry measurements one position sensitive detector is needed. The technology available today (2 mm resolution, area $400 \times 400\,\mathrm{mm}^2$) would work. But higher resolution and a wider area would improve the instruments performance. In principle the instrument could be upgraded with a *better* detector once it is available without affecting the rest of the instrument. There is no preference for any detector technology from our side. Table 2.4 gives the (realistic) wish-list of the detector properties. [→9.2]

	state-of-the-art	ideal parameters
size	$400 \times 400\,\mathrm{mm}^2$	$500 \times 170\,\mathrm{mm}^2$
resolution horizontal	2 mm	< 0.5 mm
resolution vertical	2 mm	2 mm
rate at 5 Å		$5 \cdot 10^8\,\mathrm{s}^{-1}\text{Å}^{-1}$
rate at 9.4 Å		$2 \cdot 10^8\,\mathrm{s}^{-1}\text{Å}^{-1}$

Table 2.4: Key parameters for the area detector. The numbers of the state-of-the-art detector were given by R. Hall-Wilton, ESS.

2.9.2 single detector

For diffraction measurements on the films or the substrates a second (single) detector on a shorter 2θ arm might be used. This possibility proved to be useful e.g. to check possible bending or twinning upon cooling.

2.9.3 CCD camera

To align the guide and monitor its performance, and for aligning the sample a CCD camera in front of the area detector can be used. This has the advantage that the resolution is much higher, while its draw-backs of high noise and low efficiency do not play a role for this purpose.

The active area should be some $150 \times 150\,\mathrm{mm}^2$, the resolution about $0.1 \times 0.1\,\mathrm{mm}^2$.

2.10 operation modes

In figure 2.7 the three principle operation modes are sketched, and the corresponding λ-θ detector diagrams are shown. A short description is given below, and an extensive discussion including data acquisition and reduction is given in the appendix [→10].

2.10.1 almost conventional & off-specular reflectivity

[→10.1] Though still giving a convergent beam to the sample, this mode is quite close to the operation scheme of conventional TOF reflectometers. An aperture 2.2 m before the sample defines the divergence $\Delta\theta$, the wavelength is obtained by the time-of-flight, and θ is adjusted by rocking the sample. The λ resolution is given by the pulse length and varies from 2.2% (9.4 Å) to 4% (5 Å).

Because of the disentanglement of beam spot size and divergence in the *Selene* guide, the footprint on the sample surface is defined by the aperture at $x = 28.2$ m. Over-illumination of the sample and illumination of the sample environment can be suppressed.

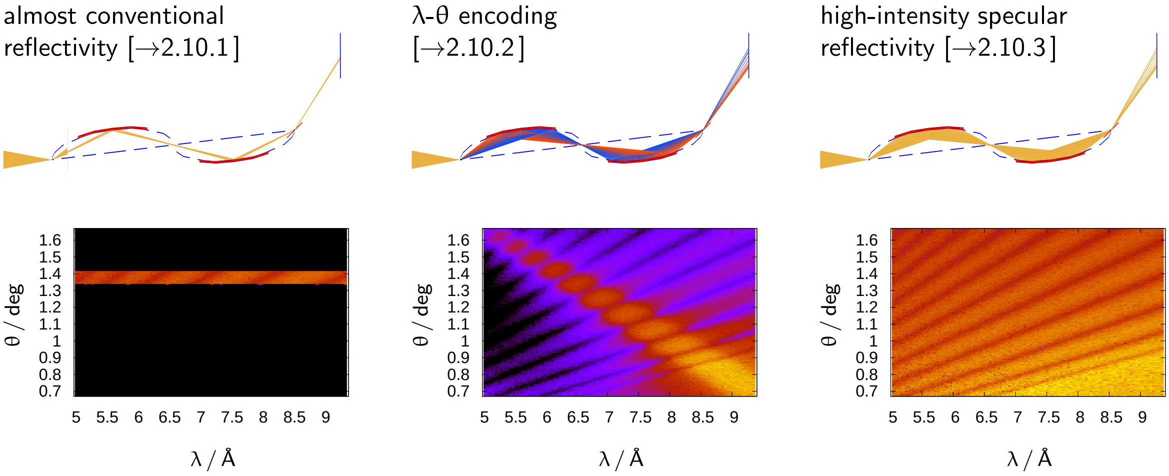

Figure 2.7: Operation schemes and $I(\theta, \lambda)$ maps obtained by simulation assuming a 1000 Å thick Ni film on glass as sample: using a slit before the sample, using a multilayer monochromator for angle-wavelength encoding, and using full divergence and pulse.

By moving the divergence-defining aperture within the divergence of the beam leaving the guide, one can change θ without tilting the sample.

Figure 2.8 shows intensity maps (left), and the reflectivity curve extracted therefrom (right). These data were obtained by simulation.

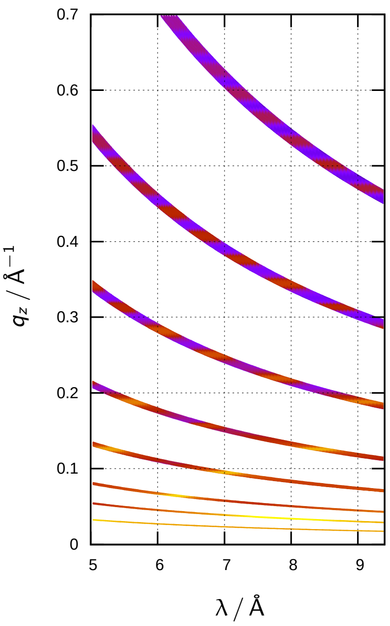

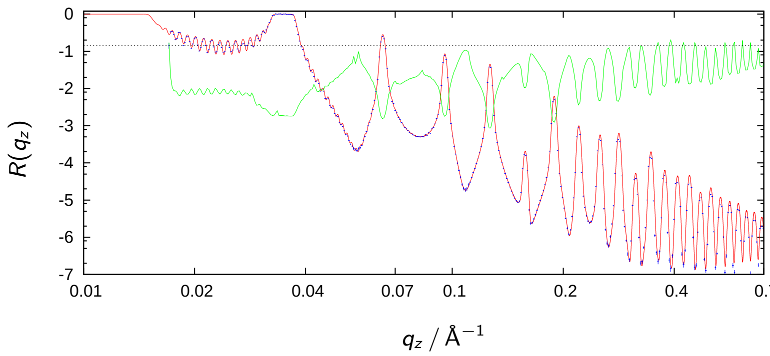

Figure 2.8: Intensity map $\log_{10}[I(\lambda, q_z)]$ for a Ni/Ti multilayer on Si obtained in the almost conventional mode [→10.1] (left). The areas correspond to the sample orientations $\omega = -0.5°$, $0.0°$, $0.6°$, $1.8°$, $3.6°$, $6.6°$, $11.3°$, and $18.8°$, respectively. The intensities are not normalised. From these maps the $R(q_z)$ curve sown above was obtained. The *measurement times* for each angular setting reach from 1 min for $\omega \leq 0.0°$ to 10 min for $\omega \geq 3.6°$.

This mode will be needed to align the sample, and for measuring (or discriminating) off-specular scattering.

off-specular scattering In this mode off-specular scattering can be measured exactly in the same way as on conventional TOF reflectometers. Without using pulse shaping choppers the q_z resolution is essentially given by $\Delta\lambda \propto \tau$. The q_x resolution varies strongly as a function of λ and θ_f.

2.10.2 angle-energy encoding

[→10.2] Compared to the almost conventional mode there are two essential differences: It allows to cover a wider q_z range in one shot by relating λ_{max} to small θ and λ_{min} to large θ. And while λ is encoded in θ, it has the resolution $\Delta\lambda/\lambda = \Delta\theta/\theta$. This means that the resolution can be manipulated without pulse shaping, so no choppers are needed.

The encoding is achieved by using a (double bounce) multilayer monochromator before $x = 28.2$ m. To get a clean beam a fast slit system 2.2 m before the sample is necessary to scan θ within one pulse.

Figure 2.9 shows intensity maps obtained by simulation for this operation scheme.

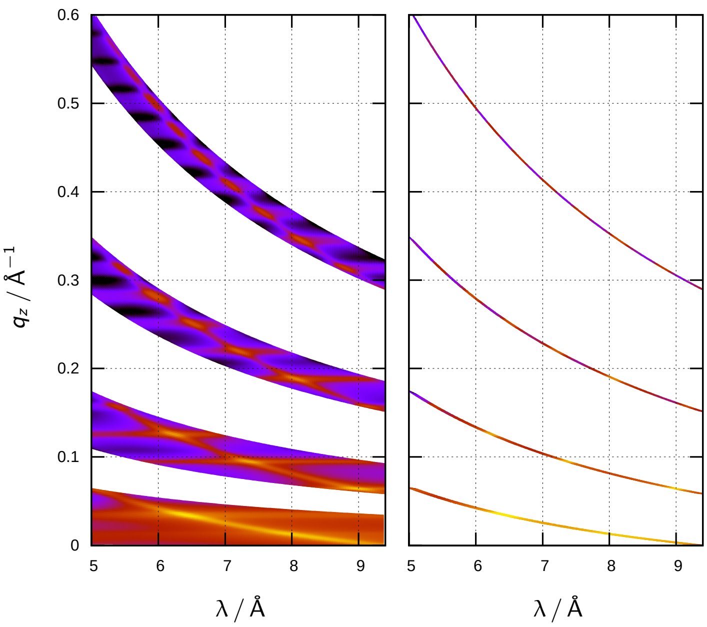

Figure 2.9: Intensity map $\log_{10}[I(\lambda, q_z)]$ for a Ni/Ti multilayer on Si obtained in the λ/θ encoding mode [→10.2]. The 4 areas correspond to the sample orientations $\omega = -0, 5°$, $2°$, $6°$, and $12°$, respectively. The intensities are not normalised. The left maps shows the signal after transformation of t to λ and θ to q_z. In the maps on the right side the areas where only off-specular intensity is expected (assuming a perfect monochromator) are shaded.

This is the mode of choice if $\Delta q_z/q_z = 3\%, 5\%, \dots 20\%$, or a wide q_z range are required.

off-specular scattering Also in this mode off-specular scattering can be measured. Since the specular scattering occupies the diagonal of the λ-θ diagram, the off-specular *area* consist of tow triangles. The q_z resolution is almost constant, the q_x resolution varies strongly as a function of λ. Figure 2.10 compares the q_x-q_z area covered by the almost conventional and the λ-θ encoding mode.

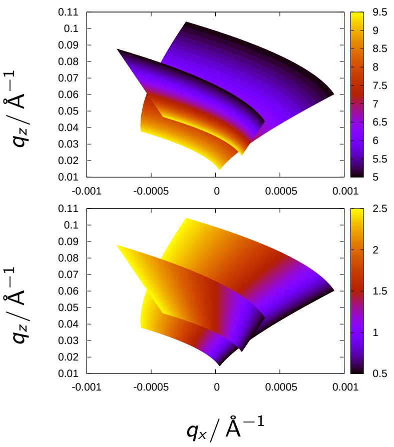

Figure 2.10: q-space covered by off-specular measurements in the λ-θ encoding mode (larger area) and in the almost conventional mode (smaller, more distorted area). In the top map λ and in the bottom map θ is plotted as a function of q_x and q_z. The detector was assumed to cover $\theta_f = 0.5°$ to $2.5°$, and $\theta_i = 1.5°$ in the conventional mode.

accuracy In the λ-θ encoding mode it is essential that the angular error induced reduction of the λ resolution is below the $\Delta\lambda/\lambda$ aimed for. The encoding is given by $\lambda = 4\pi \sin(\theta_s + \omega_m - \omega_s)/q_m$ with the coating of the monochromator having a Bragg peak at q_m, and the monochromator and sample angles $\omega_{m/s}$. An angular error $\Delta\alpha$ caused by a misaligned guide or by waviness leads to a wrong θ and thus to $\Delta\lambda \approx 4\pi \sin \Delta\alpha/q_m$. If the angular error is so large that the beam misses the sample, the error does not cause a reduction of the resolution, but it just leads to a reduction of the reflected intensity.

For a 10 mm long sample and $\omega_s = 10°$ the projected sample height is ≈ 2 mm. This corresponds to angular errors of $0.006°$ to $0.025°$ along the last guide segment, and thus to $\Delta\lambda < 0.02$ Å. This can be neglected. So in most cases an imperfect guide will result in a reduced intensity on the detector (the dark lines seen with the prototype set-up), but the encoding is still valid.

2.10.3 high-intensity specular reflectometry

[→10.3] This is the operation mode which delivers the most flux to the sample. The full divergence and also the full wavelength band accepted by the instrument are used. The wavelength is encoded in the time of flight, and thus the resolution is given by the pulse length of the source. The angular resolution is determined by the detector resolution and the sample to detector distance.

The measured signal on the position sensitive detector is a $I(t, z)$ map which can be transformed into a $I(\lambda, \theta)$ map. Each row corresponds to a TOF measurement at a given θ, and each column corresponds to an angle dispersive measurement for a given λ. I.e. one combines the two conventional reflectometry set-ups to increase the specularly reflected intensity. But a disentangling of an off-specular signal is almost impossible.

Figure 2.11 shows an intensity map obtained by simulation, which illustrates the principle and the flux gain of this mode.

Figure 2.11: Intensity map $\log_{10}[\,I(\lambda, \theta)\,]$ for a Ni/Ti multilayer on Si obtained in the high-intensity specular reflectivity mode [→10.3]. The 4 coloured area correspond to the sample orientations $\omega = -0,5^\circ, 2^\circ, 6^\circ$, and 12°, respectively. The gray-scale area are just a lead for the eye. The intensities are already normalised.

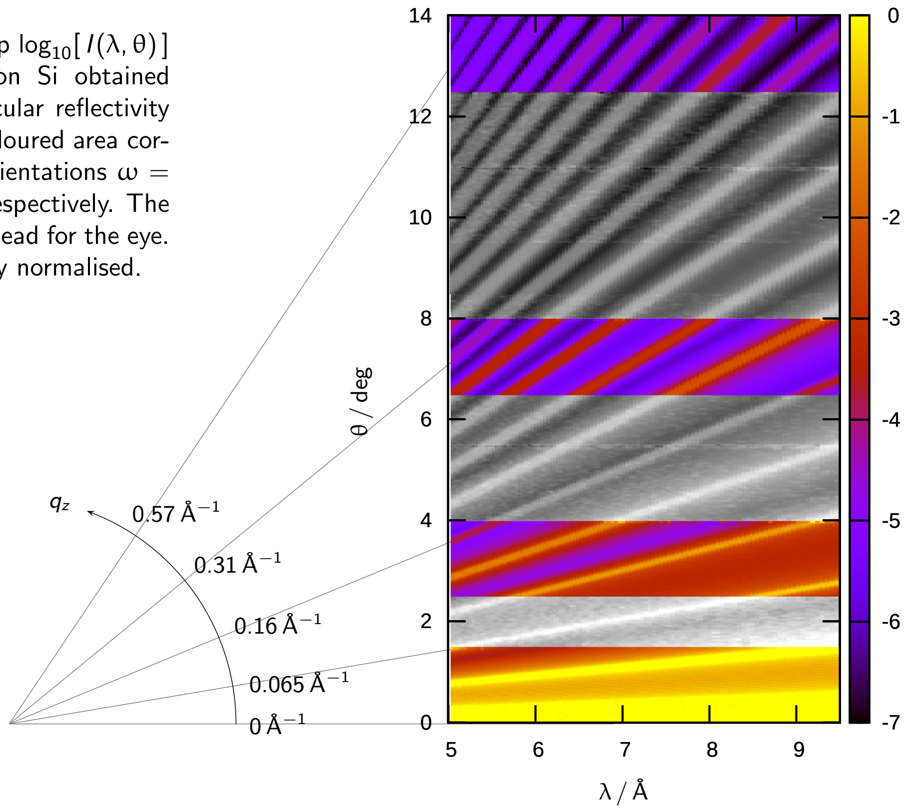

Thus this mode can be used
– on tiny samples where one is satisfied if some reflectivity curve can be obtained in a reasonable time,
– on samples with negligible off-specular or incoherent scattering,
– to screen the dependence of $R(q_z)$ on temperature, electric or magnetic fields, surface tension, or the like, and
– to perform time-resolved measurements on a s time-range.

There is no simple answer to the question of how much off-specular scattering from the sample itself, from the optical elements, or scattering from the sample environment affect the measurements. Or better the analysis in terms of specular reflectivity. But it is no problem to check this whenever necessary: A comparison of $R(q_z)$ obtained in the almost conventional mode (achieved by just closing a slit) and in the high-intensity mode immediately tells how strong the influences are.

2.10.4 further options

The following options are not yet investigated in detail. If necessary analytical or numerical simulations will be made.

focusing SANS The fact that the *Selene* guide gives a strongly focused beam can be directly used for setting up a focusing small angle scattering scheme. A detector has to be placed in the focal plane (where otherwise the sample is located), and the sample is positioned behind the guide end, some 2 m before the detector. This set-up gives an angular resolution of $\approx 0.03°$. The sample size can be up to $52 \times 52\,\mathrm{mm}^2$ (using the full divergence of 1.5° and the minimum resolution).

GISANS There are two principle modes of how GISANS could be realised. On can convert the focused beam into a parallel beam by using a parabolic reflector as sketched in figure **??**. This concept can be applied in the sample plane and in the specular scattering plane independently. The divergence of this beam is defined by the size of the virtual source. The width of the beam depends on the distance of the reflector form the focal point and can thus be tuned.

B. Hjörvarsson suggested an other approach: Using the convergent beam for GISANS results in a convolution of the detector image with the angular resolution function. While this is constant for all λ, the GISANS map on the detector scales with $1/\lambda$. Using the TOF data and the known resolution function should thus allow for a rather precise deconvolution of the detector image. Since the divergence of the incoming beam can be modified in both directions independently, one can tune the resolution function.

Rainbow The approach to spectrally analyse the reflected beam using a prism behind the sample [6, 7] can be realised if the beam is made parallel in one direction, e.g. by a parabolic reflector as described above. The detector resolution and distance allows for a high angular resolution needed for this method. The combination with TOF can be used for the measurement of inelastic processes. (The *rainbow* concept is mainly suited to reduce counting time on continuous sources.)

MIEZE A group at TUM involving R. Georgii, W. Häußler and G. Brandl investigates the possibility to use a *Selene* type guide system for a dedicated MIEZE (Modulation of IntEnsity by Zero Effort) instrument. [R. Georgii, et al.:APL, **98**, 073505, (2011)] Their know-how can be used to develop an add-on MIEZE set-up for the proposed instrument. The coils can be located before the third or fourth guide segment, and before the sample. The elliptic shape of the guide guarantees the same length for all trajectories. Figure **??** illustrates the short version of the MIEZE set-up.

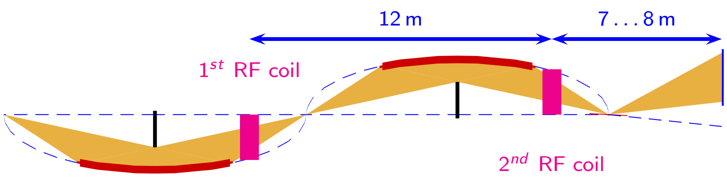

Figure 2.12: Sketch to illustrate the combination of MIEZE and a *Selene* guide.

2.11 simulations

Up to now, all simulations shown here are made using either a 1000 Å Ni film on glass, or a Ni/Ti multilayer on Si.

The simulations using reference samples are delayed due to insufficient man-power, and yet unclear boundary conditions and definitions.

It is unrealistic to perform simulations with all (fitting) reference samples, the various modes, also taking into account misalignment and off-specular scattering, plus additional simulations to highlight the instrument's strength.

Based on the parameters given in the previous section an instrument file for McStas was developed (T. Panzner) and a serious of simulations were performed.

Figure 2.7 shows sketches of the selected operation modes and the corresponding $I(\lambda, \theta)$ maps as detected with a 1000 Å Ni film on Si as a sample. The sample size was $5 \times 5\,\mathrm{mm}^2$. From these and a second set of maps obtained at a higher angle the reflectivity curves shown in figure 2.13 are obtained.

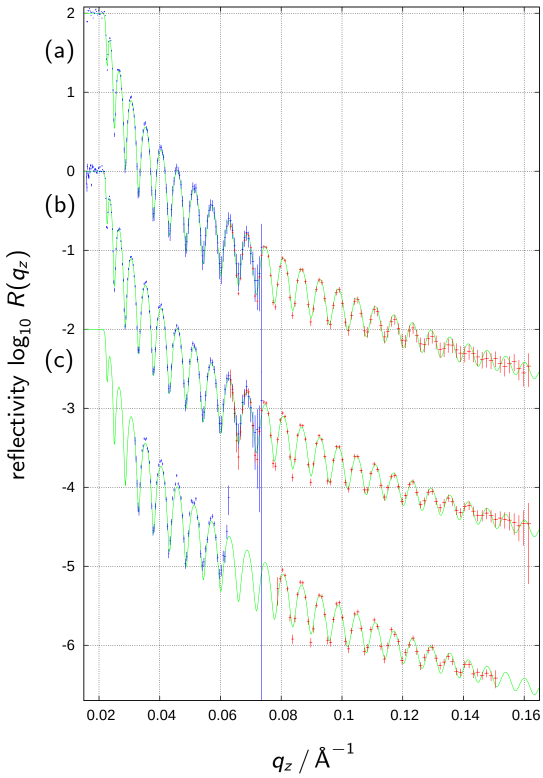

Figure 2.13: Reflectivities $R(q_z)$ extracted from the maps shown in figure 2.7 ($\omega = 2°$, blue) and from the corresponding maps for a higher angle ($\omega = 4°$, red). The corresponding modes are: (a) λ-θ encoding with $\Delta\lambda/\lambda = 3.5\%$, (b)high-intensity specular reflectivity, (c) almost conventional set up with $\Delta\theta/\theta = 4\%$. The curves are scaled by $10^2, 10^0, 10^{-2}$ for clarity. The green lines corresponds to the initial reflectivity with $\Delta q/q = 2.4\%$. The covered q_z range and the resolution functions depend on the measurement scheme. The *measurement times* t used to obtain the error bars are

mode	ω	t
(a)	2°	60 s
	4°	900 s
(b)	2°	1 s
	4°	10 s
(c)	2°	10 s
	4°	100 s

a) λ-θ encoding [→2.10.2] by using a ML monochromator after the beam extraction.

   This results in a diagonal streak in the λ/θ space, where $\Delta\lambda/\lambda = \Delta\theta/\theta =$ const. In the off-diagonal region the finite reflectivity of the ML monochromator leads to some structured background. This does not affect the specular reflectivity, but it might prohibit off-specular measurements.

b) High-intensity specular reflectometry [→2.10.3] by substituting the ML monochromator by a supermirror.

   Here the all of the available λ/θ space is used for specular reflectometry. Off-specular and incoherent scattering leads to an enhanced background. This mode allows for a fast (and dirty) screening of external parameters as e.g. temperature or magnetic field strength, and for time-resolved studies.

c) Almost conventional reflectometry [→2.10.1] by using a slit to cut down the divergence given by the set-up (b).

   The specular reflectivity concentrates on one line, while the rest of the λ/θ space is available for off-specular measurements. The q_z range accessible this way is reduced. A movement of the slit between pulses can be used to vary θ without tilting the sample.

Form these maps the reflectivity curves shown in figure **??** were obtained by integrating the λ/θ maps along constant q_z. The binning was done with $\Delta q_z/q_z = 1\%$. The error-bars shown were obtained by assuming $\Delta I/I = \sqrt{I}$ where I is the flux given by the simulation, multiplied by a *measurement time* t. For the high-intensity specular reflectivity at the lowest angle $t = 1$ s was chosen, the other values were adjusted to get comparable accuracy.

2.12 performance

The following list is a comparison of the instrument's performance to the specifications of the STAP

- sample size: $= 5 \times 5\,\text{mm}^2$ taking into account sample environments

→ The complete instrument is optimised for sample sizes below $10 \times 10\,\mathrm{mm}^2$, down to below $1 \times 1\,\mathrm{mm}^2$. It is possible to define an accurate footprint on the sample surface without penumbra.

Samples wider than 10 mm and longer than 40 mm can not be homogeneously illuminated.

- wavelength resolution: up to 10% $\Delta\lambda/\lambda$ with options to increase to 1%, 3% or 5%.

→ The intrinsic λ-resolution gives $\Delta\lambda/\lambda = 2\%$ to 4% without beam manipulation. The requested resolution of 10% can thus not be realised via TOF. In the λ-θ encoding mode, this is possible.

A resolution $\Delta\lambda/\lambda = 1\%$ for small q_z is not possible due to the expected detector resolution.

A constant $\Delta\lambda/\lambda$ ranging from 2% to 20% will be realised in the λ-θ encoding mode, only.

- Minimum $q$range:$0.005\,\text{Å}^{-1} < q < 0.5\,\text{Å}^{-1}$ measurable in 3 to 4 angles of incidence

→ This requirement is easily matched. The upper limit is $q_z = 2\,\text{Å}^{-1}$ given by the highest reasonable detector angle.

For $q_z \approx 0\,\text{Å}^{-1}$ the resolution requirements can not be fulfilled. Otherwise this region is accessible.

- low background: reflectivities = 109 measurable

→ One big advantage of the *Selene* guide system is that it transports much less neutrons compared to other guides. This and the focusing to the sample should lead to a lower background and to a reduced illumination of the sample environment.

A quantitative discussion is almost impossible.

- polarisation/polarisation analysis

→ Full polarisation is a key-feature of the proposed instrument. There are various ways to polarise and to analyse the beam, all are well established so that there is no risk related.

High magnetic fields at the sample position are possible. There is free space with a radius of more that 2 m available without any optical or mechanical component. Polariser and analyser can be located 12 m, and 6 m from the sample, so that an interaction with the sample field can be avoided.

- a GISANS collimation option and variable detector distance up to 15 m.

→ This requirement is not matched. And it is ill-defined. The 15 m are needed for using a collimation system to *focus* the beam. For the proposed instrument this is already (and better) realised by the guide. Though not optimised for GISANS, one can in principle perform such measurements using a detector at the focal plane and by positioning the sample at the guide exit. This has not yet been studied in detail.

An important feature, not mentioned in this list is the minimum counting time, so that time-resolved measurements are possible. In the high-intensity mode a *blurred* resolution and an eventually complex background (off-specular and incoherent scattering) are accepted to increase the flux by at least one order of magnitude. This allows for measurements in the sub-second range for moderate q_z. counting time

3 Technical Maturity

[3 pages] [Identify key components that define the instruments performance and whether the functional requirements can be met with existing technology. If additional development is required, present a plan for the development and the technological risks associated. Present an appropriate risk mitigation strategy.]

3.1 guide system

The biggest challenge of the presented instrument is the long-term stability of the *Selene* guide alignment. It is relatively straight forward to set up and align the individual components, as long as one has full access. Once burrowed under concrete and activated, this is no longer the case for the 1^{st} guide section.

A misalignment of the 1^{st} guide section as a whole can be accepted if the pin-hole in the extraction unit is large enough to act as a virtual source also for the tilted or shifted guide. The misalignment of individual components is easy to trace, but not so easy to correct. A solution would be to putt all components on actuators But this would result in ≈ 150 degrees of freedom — which is essentially a costing problem. The realignment with these actuators is possible by using light optics or interferometry and an adapted computer algorithm. Tests to align the prototype elements with an interferometer started in 04. 2013.

guide accuracy The angular accuracy needed for the guide alignment can be estimated by looking at the longest free flight path before the sample. I.e. the trajectory from the entrance of the last guide segment to the sample. A beam off-set of 0.1 mm at the sample position corresponds to an angular error of $0.1\,\text{mm}/9600\,\text{mm} \approx 10^{-5}$ rad. The waviness of a state-of-the-art float glass guide is of the order $5 \cdot 10^{-5}$ rad. A yz position accuracy better than 0.1 mm can be achieved, so that this can be neglected compared to the influence of waviness. An orientation error of 10^{-5} rad corresponds to an displacement of the 500 mm long guide element of 5 µm. This is a manageable quantity.

monitoring The geometry of the *Selene* guide allows for a relative simple monitoring of the guide alignment. A point-like white light source (e.g. a LED) at the initial focal point of one segment should ideally produce a homogeneous rectangular image on a screen behind the final focal point. Any deviation of the guide surface from the exact elliptic profile leads to a redistribution of the intensity on the screen. Since there is a unique relation of any point on the screen to certain beam trajectory, it is possible to trace a intensity drop back to the part of the guide which is misaligned.

By coupling in/out the light by optical mirrors (e.g. Si wafers), this monitoring set-up can be installed permanently, allowing for a fast feedback.

Instead of using a point-source and a screen, it is also possible to use an interferometer and a spherical mirror. This approach is currently investigated at the inspection lab at SLS, PSI.

Open topics:
– fast feedback,
– radiation damage of actuators

3.2 optical components, polarisation

A prototype of a frame-overlap-filter / polariser working in transmission [→7.1] will be tested in 5. 2013 at PSI. The double bonce monochromator was already successfully tested [→**??**].

Spin analysers using supermirror technology to cover a wide angular range or a large window are operational, e.g. at FOCUS, PSI, or at HYSPEC, SNS.

3.3 mechanics, sample stage

The mechanical support system for the sample and sample environment, and the analog support for the virtual source are standard components. The same is true for slow slit systems, and for stages to exchange optics or insert a CCD camera.

A challenge is the support system for the 2$^{\text{nd}}$ *Selene* guide section. This is some 20 m long, but it has to be adjusted with respect to the virtual source with an accuracy in the sub-mm range and an angular error well below 0.1°. Since it is expected that the heavy shielding leads to a drop of the monolith area, it is necessary that the guide can be realigned as a hole, without too much effort.

3.4 fast slit system

For all operation modes a slit behind the last guide segment is needed. For the almost conventional mode it defines the beam divergence and the angle of incidence, for all modes it helps aligning the sample. Such a slit is a standard component.

If one wants to switch the slit position and opening in between pulses, it must be able to change the blade positions by up to 60 mm within 10 ms. If this is not possible one looses several pulses and thus time-resolved measurements might suffer.

When used to scan the beam during one pulse, both blades must move independently and very accurate over $\approx$ 60 mm within 60 ms and reset within 10 ms. This would allow to cut down unwanted scattering from the monochromator in the λ-θ encoding mode. If such a device is possible to realise is not clear. It was discussed with T. Gahl, ESS, but yet there is no clear conclusion so that further clarification is needed.

3.5 detector

The detector technology available nowadays can be used in principle, so that even when new concepts fail, the operation of the instrument is guaranteed. The limitations of present days detectors are the resolution, the size and the accepted count rate.

In section 9.2 a wish-list of the detector properties is given together with the motivations.

This wish-list was sent to R. Hall Wilton and to H. Wacklin, both ESS, on February 2013 with the request to comment on it (reminder in May). There is no feed back up to now.

Besides the additional costs for a new detector, there are no principle obstacles to replace the *day one* detector for a better one later.

3.6 computing, data analysis

The raw data will have a format of the type $I(t, y, z)$ (or the single event analog). Simple perl scripts to normalise, integrate and re-bin the data are written for the analysis of the prototype measurements. This means that the algorithms for data analysis are available.

The situation changes when one wants to conserve all information contained in the raw data for fitting. The re-binning and integration (especially in the high-intensity mode) leads to a reduction and mixing of resolution. To overcome this, one can compare measured and simulated intensity maps, rather than curves. The challenge is then to modify the output of a simulation program (eventually supported by reference measurements), and to implement a good fitting algorithm. The fitting *by eye* is no longer possible.

4 Costing

[2 pages] [Present a preliminary cost estimate broken down by project phase and cost category including both capital and personnel costs following relevant ESS costing guidelines. Define the categories clearly and state what the estimate was based on (e.g. estimate by an ESS technical group).]

This is just a collection of cost estimates we got up to now. No man-power is included. No scheduling. We will take care of the ESS costing guidelines in the future.

The costs given below for some selected components of the instrument are based on requests to the manufacturer, on price lists and on feedback by the ESS. They display the situation beginning 2013.

4.1 insert in the extraction unit and instrument shielding

The measures and materials used for this estimate are based on input by P. Bentley, ESS, 10. 04. 2013.

The insert within the target monolith is assumed to consist of copper. Its measures are: $0.2 \times 0.2 \times 4.0\,\mathrm{m}^3 = 0.16\,\mathrm{m}^3 \mathrel{\hat{=}} 1.4\,\mathrm{t}$ (the free space of the beam can be neglected, here).

The masks at 18.6 m and at 26 m and between monolith and common shielding are assumed to use $1\,\mathrm{m}^3$ copper, each. This corresponds to 27 t.

Assuming a copper price (04. 2013) of 6 k€/t this gives 170 k€.

The instrument shielding (without the common shielding) from $x = 15\,\mathrm{m}$ to $x = 25.8\,\mathrm{m}$ is assumed to have a heavy concrete core with a cross section of $2 \times 2\,\mathrm{m}^2$ (with the guide in the centre), and an outer shell of light concrete with a cross section of $5 \times 5\,\mathrm{m}^2$. This corresponds to $44\,\mathrm{m}^3$ of heavy concrete, and $226\,\mathrm{m}^3$ of light concrete. A recent (01. 2013) offer to PSI for $200\,\mathrm{m}^3$ light concrete and $50\,\mathrm{m}^3$ heavy concrete summed up to 2 000 k€ (without form factor or reinforcement).

The common shielding up to $x = 15\,\mathrm{m}$ is not taken into account.

insert and instrument shielding	2 200 k€

4.2 guide

SwissNeutronics made an offer for the *Selene* neutron guide and the support system on January 2013. This offer fits the parameters for the double-*Selene* guide system as discussed in section 2.2.

The offer covers the neutron guide on glass or aluminium, the alignment frames, granite beams as a base and an aluminium housing to contain the vacuum. This does not exactly match the requirements by the ESS, since shielding issues most likely will not allow for the offered wide and straight vacuum housing and the alignment system with frames. But it still gives an idea of the actual costs to be expected. For the guides the offer covers the curved substrates with a $m = 2.5$ Ni/Ti coating. In detail there are 4 guide sections of 7.2 m, each, consisting of 15 elements, made up of 2 truly curved mirrors.

double-*Selene* guide system	550 k€

4.3 guide support

The support consists of 4 granite beams on kinematic mounts, the alignment frames, the vacuum housing, and vacuum windows. No shielding is included. Mounting is due to the customer.

guide support	520 k€

4.4 mechanics (sample stage and the like)

Request to Peter Keller, LDM mechanics, PSI, on 26. 03. 2013.

motion mechanics ??? k€

4.5 motion control

(discussed with T. Gahl, ESS, 18. 03. 2013) For the *standard* components (i.e. without fast aperture [→**??**]) an approximate price per freedom of 4 k€ is assumed, including motor controller, encoder, motor, and cabling. This leads to

motion control 150 k€

4.6 detector

Request to Richard Hall-Wilton, ESS, on 20. 02. and on 19. 03. 2013.

monitor [to be done]

A CCD camera with scintillator and housing for instrument and sample alignment (based on a similar system purchased for BOA at PSI) costs ≈ 60 k€.

detectors ??? k€

4.7 filter / polariser

Based on the costs of a prototype of the bent frame-overlap and polarisation filter, a similar but longer device will cost some 25 k€.

The price for one RF flipper (electronics, coils, magnets and housing) is approximately 30 k€ (private communication with P. Hautle, PSI).

analyser (Uwe) [to be done]

polarisation equipment ??? k€

5 List of abbreviations

physical quantities	
x	lab-system: horizontal scale, *along the main neutron path*
y	lab-system: horizontal scale, normal to x
z	lab-system: vertical scale
t	time, with $t = 0$ at the beginning of a neutron pulse
τ	(≈ 2.8 ms) length of the proton pulse
T	($= 70$ ms) pulse repetition time
λ_{min}	shortest wavelength used for measurements
λ_{max}	longest wavelength used for measurements

ellipse parameters describing the guide geometry	
a	long half-axis
b	short half axis
c	($= a^2 - b^2$) distance from focal point to center
b/a	asymetry of ellipse
α	angle between long axis and end of guide seen from the first focal point
β	angle between long axis and beginning of guide seen from the first focal point
$\Delta\theta$	($= \beta - \alpha$) accepted divergence of the guide
ϵ	($= \beta/2 + \alpha/2$) inclination of the long axis relative to the mean beam direction
ξ	length of the guide relative to the distance between focal points

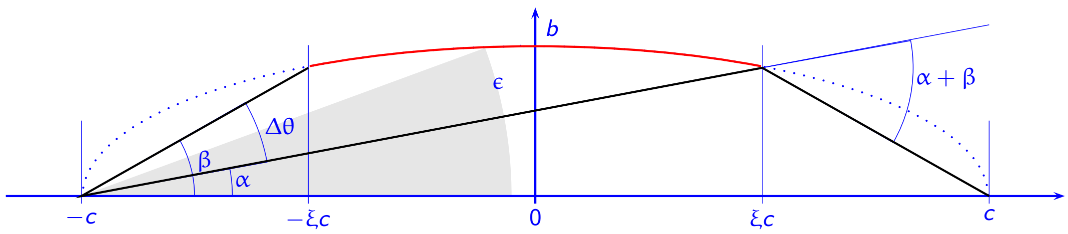

nomenclature for positions along the guide	
P_i	first focal point of guide section i
P_{i+1}	second focal point of guide section i, and first focal point of guide section $i+1$
P_5	..., and sample position

sample coordinate system	
ω	inclination of the sample surface relative to the long axis of the last guide, in the scattering plane this is a pure instrument parameter and is only indirectly connected to the angle of incidence!
θ_i	actual angle of incidence of a neutron on the sample surface
θ_f	final angle of a neutron leaving the sample surface

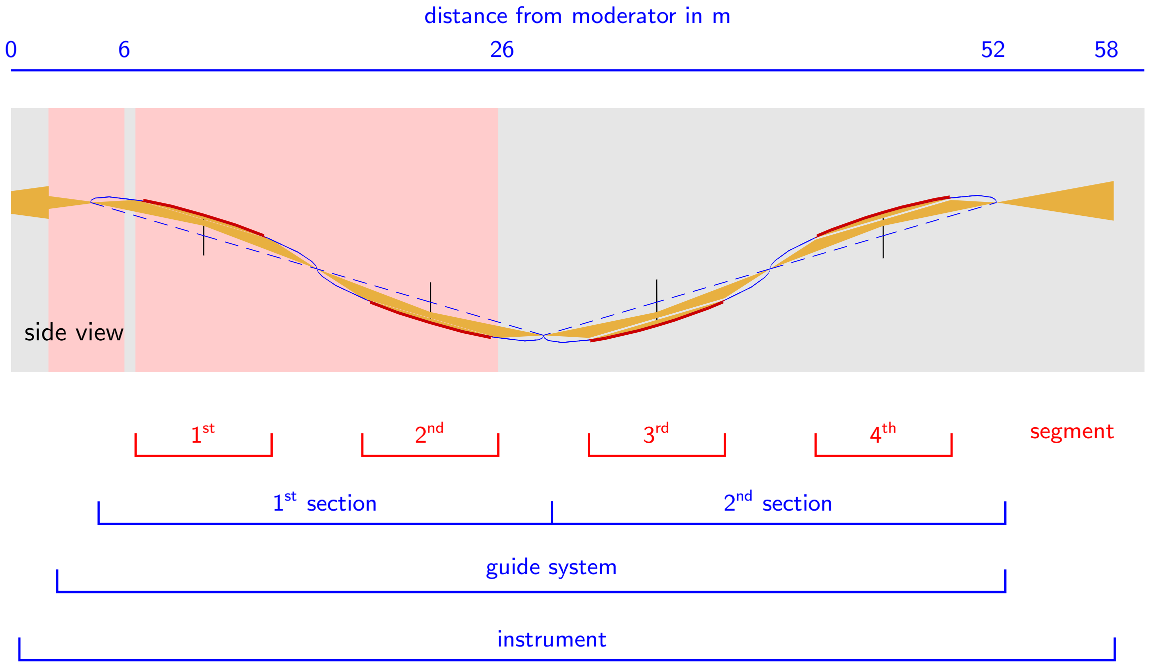

Figure 5.1: Nomenclature used in this script to adress the various items and measures of the double *Selene* guide. The sketch is taken from figure 2.1. The guide segments are the elliptically curved and SM coated guides. The distance between the initial and final focal point of one *Selene* guide is called section. Here, two sections and the extraction unit make up the guide system, ending at the sample position.

6 the Selene guide system

We chose two subsequent elliptically shaped reflectors to focus the beam to the sample. The reason is that this set-up allows for

- independent definition of the divergence $\Delta\theta$, and of the beam spot size at the sample;
- a three-dimensional definition of the footprint;
- convenient beam manipulation;
- early reduction of the phase space, i.e. low background and radiation in the sample and detector region.

At the same time all trajectories have the same length. In the following subsections several aspects of the *Selene* guide system are presented.

The design and a large part of the optimisation of the *Selene* guide system was performed analytically. This is possible because of the rather straight-forward and clear mathematical description of the possible beam trajectories. As a consequence one can relate allmost all geometrical parameters of the guide system, the coating and the transmission. The rather large number of parameters collapses this way to essentially three which can be chosen freely. All the rest is then determined. In the following sections these relations are derived and discussed.

Figure 6.1 illustrates the approach chosen here for the design the instrument, starting with some guess for the desired divergences and wavelength-range at the sample position. The second set of input parameters are the given source brightness $I_0(\lambda)$ and a reasonable length of the guide, described by the ration of the actual guide segment length to the focal ponit distance, ξ. As figure of merit the measurement time t is used. The physical parameters of the guide (b/a and ϵ) are deduced from the starting parameters and they determine the coating (m), reflectivity (R) and thus the transmission T of the guide. Togther with the divergence and $I_0(\lambda)$ this determines the counting time.

The *optimisation problem* can be illustrated at the example of $\Delta\theta$, which enters the counting time quadratically (for high-intensity specular reflectivity), but which also affects m linearly. Since high m leads to a lower transmission T with a more complicated dependence, one has to iteratively find the best $\Delta\theta$.

history

The idea for the *Selene* guide is based on concepts of F. Ott to use a focused beam with a wide divergence, and in combination a λ-θ encoding obtained by a graded monochromator of half-elliptic shape.[8, 9] First experiments with a graded multilayer coating [10] revealed conceptual problems and led to the approach to use a flat multilayer monochromator for λ-θ encoding, followed by the elliptic reflector. And attempts to correct for coma aberration finally led to the *Selene* guide geometry with two subsequent elliptic reflectors. This way, neutron guide and encoding are decoupled. I.e. encoding is optional and might be also achieved by other approaches like the *rainbow* concept by R. Cubitt.[6, 7]

Though developed for a reflectometer, the *Selene* guide concept can in principle used also for other instruments. The limiting factors are the transported divergence, the minimum wavelength, and the sample size.

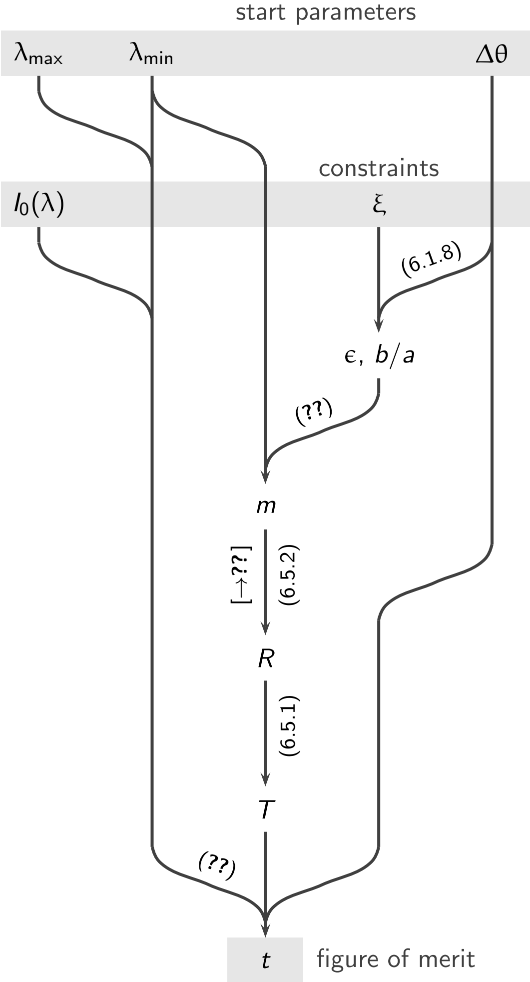

Figure 6.1: Flow diagram used to estimate the counting time t as a figure of merit from chosen (λ-range, $\Delta\theta$) and given ($I_0(\lambda)$, ξ) start parameters.
The meaning of the other symbols is: ϵ, b/a orientation and shape of the ellipses, m coating of guides, R reflectivity of the guide, and T transmission of the guide system.
The diagram is simplifyed since it is based on the ideal assumption of a point-like sample, perfect guides and coatings, and some external constraints as the exclusion of the prompt time for data collection [→**??**] are not taken into account.

6.1 geometrical considerations for an elliptic reflector

The geometry of the elliptic guides (i.e. the ratio of the half axes b/a), their length and coating should be defined starting by the requirements at the sample position. The limitations are the maximum curvature of the guide, the available coating, $I_0(\lambda)$, and the space available.

The following formulae can be used to estimate the optimum geometry of a *Selene*-type guide for given parameters like expected divergence $\Delta\theta$, and wavelength range $\lambda_{min} \ldots \lambda_{max}$.

Theses formulae are based on the small-angle approximation $\tan\alpha \approx \alpha$, $\tan\beta \approx \beta$, a strong asymmetry of the ellipse $a \gg b \Rightarrow c \approx a$, and a symmetric guide.

ellipse relation:

$$\begin{aligned}
\frac{x^2}{a^2} + \frac{y^2}{b^2} &= 1 \\
y &= \pm\frac{b}{a}\sqrt{a^2 - x^2} \\
c &= \sqrt{a^2 - b^2} \qquad \text{half distance between focal points}
\end{aligned}$$

minimum acceptance angle (relative to long axis):

$$
\begin{aligned}
\alpha &\approx \frac{b}{a}\frac{\sqrt{a^2-(\xi a)^2}}{(\xi+1)a} \\
&\approx \frac{b}{a}\sqrt{\frac{(1-\xi)(1+\xi)}{(1+\xi)^2}} \\
&\approx \frac{b}{a}\sqrt{\frac{1-\xi}{1+\xi}} \\
&\approx \frac{b}{a}\frac{1-\xi}{\sqrt{1-\xi^2}} \qquad (6.1.1)
\end{aligned}
$$

maximum acceptance angle (relative to long axis):

$$
\begin{aligned}
\beta &\approx \frac{b}{a}\frac{\sqrt{a^2-(\xi a)^2}}{(\xi-1)a} \\
&\approx \frac{b}{a}\sqrt{\frac{(1-\xi)(1+\xi)}{(1-\xi)^2}} \\
&\approx \frac{b}{a}\sqrt{\frac{1+\xi}{1-\xi}} \\
&\approx \frac{b}{a}\frac{1+\xi}{\sqrt{1-\xi^2}} \qquad (6.1.2)
\end{aligned}
$$

accepted / delivered divergence:

$$
\begin{aligned}
\Delta\theta &= \beta-\alpha \\
&\approx \frac{b}{a}\left(\frac{1+\xi}{\sqrt{1-\xi^2}}-\frac{1-\xi}{\sqrt{1-\xi^2}}\right) \\
&\approx \frac{b}{a}\frac{2\xi}{\sqrt{1-\xi^2}} \qquad (6.1.3)
\end{aligned}
$$

inclination of the center of the beam relative to the long half axis:

$$
\begin{aligned}
\epsilon &= \frac{1}{2}(\alpha+\beta) \qquad (6.1.4) \\
&\approx \frac{1}{2}\frac{b}{a}\left(\frac{1+\xi}{\sqrt{1-\xi^2}}+\frac{1-\xi}{\sqrt{1-\xi^2}}\right) \\
&\approx \frac{1}{2}\frac{b}{a}\frac{2}{\sqrt{1-\xi^2}} \\
&= \frac{\Delta\theta}{2\xi} \qquad (6.1.5)
\end{aligned}
$$

minimum coating of the guide surface:

$$
\begin{aligned}
m &= \frac{4\pi\,\frac{\alpha+\beta}{2}}{\lambda_{\min}\, q^{c}_{\mathrm{Ni}}} \qquad \text{with (6.1.4):} \\
&= \frac{4\pi\,\epsilon}{\lambda_{\min}\, q^{c}_{\mathrm{Ni}}} \qquad (6.1.6)
\end{aligned}
$$

Starting with input parameters $\lambda_{\min}$ and $\Delta\theta$ required at the sample, and with ξ it is possible to deduce all other paramters:

$$
\frac{b}{a} \approx \frac{\Delta\theta}{2}\sqrt{\frac{1}{\xi^2}-1} \qquad (6.1.7)
$$

$$
\epsilon \approx \frac{\Delta\theta}{2\xi} \qquad \text{inclination of the guide, and maximum angle of incidence on the guide} \qquad (6.1.8)
$$

$$
m = \frac{4\pi\,\epsilon}{\lambda_{\min}\, q^{c}_{\mathrm{Ni}}} \qquad \text{for a finite source, the angular error has to be taken into account to calculate the } \textit{real } m \qquad (6.1.9)
$$

and

$$\alpha \approx \epsilon \cdot (1 - \xi) \tag{6.1.10}$$
$$\beta \approx \epsilon \cdot (1 + \xi) \tag{6.1.11}$$

For $\Delta\theta \approx 2\epsilon$ the pre-assumptions are no longer fulfilled! A reasonable upper limit for ξ is about 80%.

Example:
$m = 5$ and $\lambda_{\mathrm{min}} = 3$ Å gives $\epsilon = 1.5°$ and

$\Delta\theta$	ξ	b/a
1.0°	33%	0.025
1.5°	50%	0.023
2.0°	66%	0.020
2.5°	83%	0.014
3.0°	100%	0.000

Figure 6.2 shows the iso-lines for constant m and for constant $\Delta\theta$ on a map of b/a vs. ξ, obtained for $\lambda = 4$ Å. E.g. if a divergence of $\Delta\theta > 3°$ is required, but the coating is limited to $m = 6$ the possible values for b/a and the relative length ξ are within the (light gray) area below the blue iso-line for $m = 6$ and above the red iso-line for $\Delta\theta = 3°$. So the smallest xi is ≈ 0.62 with the strong curvature $b/a \approx 0.033$. Relaxing the latter value leads to a longer guide and allows for a coating with lower m.

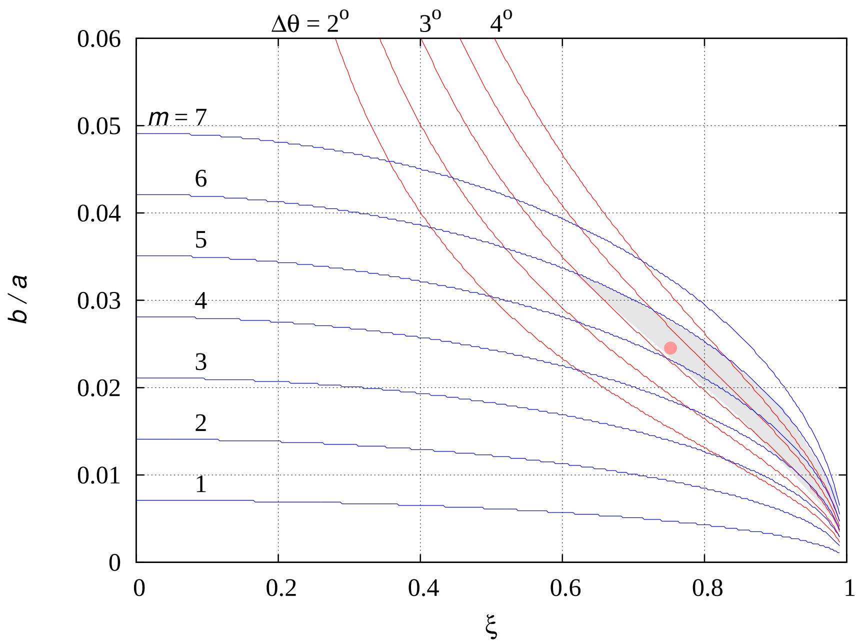

Figure 6.2: Iso-line for constant m (blue) and for constant divergence $\Delta\theta$ (red) for $\lambda = 4$ Å as a function of the length of the guide and the ratio of the half axes parameters b/a.

Reducing the wavelength e.g. from 4 Å to 2 Å does not affect the red iso-line, but the blue ones are scaled down by 0.5 along b/a. There is no intersection left (for reasonable guide lengths) with the $\Delta\theta = 3°$ criterion, so that there is no guide geometry possible fulfilling the requirements.

For $\Delta\theta = 3°$ and $\lambda = 4$ Å a reasonable choice would be $b/a \approx 0.025$ and $\xi = 0.75$ (marked by a red dot). The coating then should be $m \approx 5.5$.

6.2 angular acceptance

We are often confronted with the remark that a full ellipse could transport twice the divergence of half an elliptic guide. The point is that the divergence should be defined by the needs on the sample, or it is given by geometrical limitations. In this case one has to ask for the most efficient way to transport this divergence.

And if this can be realised with one branch of an ellipse, there is no need to accept the disadvantages of the full ellipse.

For a given $\lambda_{\min}$ and $\Delta\theta$ there is only one degree of freedom left to define all geometrical parameters of the ellipses and the coating [→**??**]. For a reflectometer one can obtain approximately an optimum set of $\Delta\theta$ and m when optimising for brilliance transfer [→**??**]. The characteristic measures of the guide then are

$$\text{maximum incident angle on guide = inclination of the ellipse} \quad \epsilon \approx \frac{\lambda_{\min}\, m q^{c}_{\mathrm{Ni}}}{4\pi} \tag{6.2.1}$$

$$\text{length of the reflector relative to } 2a \quad \xi \approx \frac{\Delta\theta}{2\epsilon} \tag{6.2.2}$$

$$\text{asymmetry of the ellipse} \quad \frac{b}{a} \approx \sqrt{\epsilon^2 - \Delta\theta^2/4} \tag{6.2.3}$$

So besides for the length $4c$, the guide system is defined.

6.3 coma aberration — and correction

Elliptic reflectors show coma aberration. This means two things: radiation emitted from (close to) the first focal point into a solid angle Ω and reflected before the mid of the ellipse reaches the second focal point under a smaller solid angle. Radiation emitted in Ω but reflected behind the mid of the ellipse result in a large solid angle. I.e. The focusing / de-focusing property of the reflector varies along its length.

At the same time the position of the image of an off–axis pre-image point depends on the position where along the reflector the beam is reflected. For an early reflection the distance of the image from the long axis increases, for a late reflection it decreases.

In total the phase space density is conserved, but the distribution intensity vs. angle and beam-height $I(\theta, z)$ is distorted.

For geometries and reflection angles typical for neutron guides one can estimate the image size as a function of the initial slit size z_1 and the angle α_2 between the reflected beam and the long axis of the ellipse:

$$z_2(\alpha) \approx z_1 \frac{(b/a)^2}{\alpha_2^2} \tag{6.3.1}$$

An identical second collinear reflector, sharing one focal point with the first one shows the same aberration, but since early reflection in the first reflector leads to a late reflection in the second one, the distortion is almost cancelled.

Analytically this can be shown by using eqn. 6.3.1 and $\alpha_2\alpha_1' = \alpha_3\alpha_2' = (b/a)^2$, $\alpha_2 = \alpha_2'$. For the final image z_3 one gets

$$z_3(\alpha_3) \approx z_2(\alpha_2)\frac{(b/a)^2}{\alpha_3^2} \approx z_1 \frac{(b/a)^2}{\alpha_2^2}\frac{(b/a)^2}{\alpha_3^2} \approx z_1 \tag{6.3.2}$$

This is illustrated in figure 6.3. The maps show $I(\theta, z)$ as accepted by the elliptic reflectometer (left), the corresponding intermediate image with the distorted shape (middle) and the almost restored shape at the image (source) position. The deviations still visible originate from the final length of the second reflectometer, and from the quite large pre-image chosen to emphasise the effect of coma aberration.

It is not always useful to correct for coma aberration: If e.g. a small beam is required, on can reach this by using the beam reflected at the end of the reflector. For the presented case its height is 30% of the initial slit, only. On the other side one can get a wide beam of low divergence by using the beginning of the reflector, only. This is what at synchrotron sources is achieved with a Kirkpatrick-Baez optics (which consists of two elliptically shaped reflectors, one for each direction).

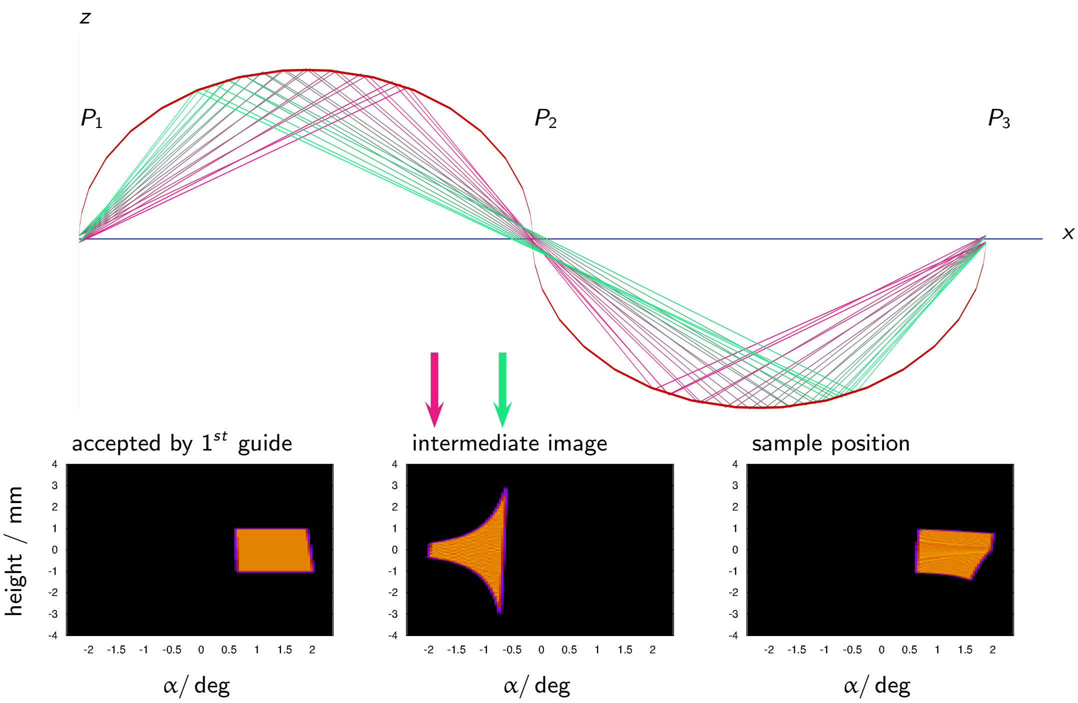

Figure 6.3: Sketch to illustrate the effect of coma aberration. The pre-image consists of 2 point-sources, located at $z = \pm 1\,\mathrm{mm}$. The half-axis parameters used here are $a = 2000\,\mathrm{mm}$, $b = 50\,\mathrm{mm}$, the sketch is stretched by 30 normal to the long axis. The take-off angle α is encoded in the colour of the beam. At the intermediate position a clear separation of the colours can be seen. High α result in an almost parallel wide beam, while low α result on a beam focused to the second focal point. Behind the second ellipse, the initial image is almost restored. The $I(\alpha, z)$ maps illustrate the shape of the phase space as accepted by the ellipse and defined by a 2 mm slit at P_1 (left), at the intermediate position P_2 (middle), and finally after correction at P_3 (right). The arrows atop the middle map denote for which α the beam is compressed (red) or expanded (green).

6.4 chromatic aberration due to gravity

P. Korelis, E. Rantsiou

While the focusing properties of reflecting optics are achromatic (besides the λ dependent reflectivity) for straight trajectories, there are chromatic effects induced by gravity. Its influence on the spot size and divergence is not immediately apparent because there are amplifying and compensating aspects for reflections on an elliptic guide. E.g. if one assumes the first reflection pointing downwards, gravity leads to a longer free flight path before the neutron hits the reflector. But it will hit it at a smaller angle.

The drop of the neutrons due to gravity is given by

$$\begin{aligned}
\Delta z &= -\frac{1}{2}\, g\, t^2 \\
g &\approx 9.81\,\mathrm{m/s^2} \\
t &\approx 2.52 \cdot 10^{-4}\,\mathrm{s\,m^{-1}\,\text{Å}^{-1}}\, x\, \lambda \\
\Rightarrow \frac{\Delta z}{\mathrm{m}} &\approx 3.07 \cdot 10^{-7} \left(\frac{x}{\mathrm{m}} \frac{\lambda}{\text{Å}} \right)^2
\end{aligned}$$

So Δz scales with distance and wavelength squared.

Δz	$x = 2400$ mm	9600 mm	19200 mm
$\lambda = 5.0$ Å	-0.04 mm	-0.7 mm	-2.8 mm
9.4 Å	-0.16 mm	-2.5 mm	-10 mm

The main question to be answered then is whether or not gravity sets limitations to the focusing performance of a *Selene* guide at the sample position. To elucidate the effect of gravity, virtual studies using the McStas simulation software package have been performed.

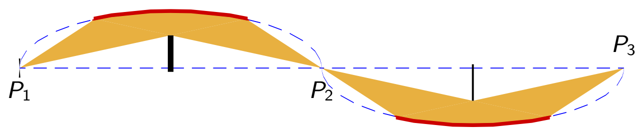

Figure 6.4: Sketch of the setup used for simulations including gravity. The guide parameters are $c = 10\,000$ mm, $b/a = 0.0228$ and $\xi = 0.5$. The initial slit has a height of 1 mm and is centred at the focal point.

The model instrument is comprised of a single *Selene* guide with the first element reflecting downwards and the second reflecting upwards as shown in figure 6.4. The geometrical parameters are the same for the horizontal (xy plane) and vertical (xz plane) elliptic reflectors: $b/a = 0.0228$, $\xi = 0.5$, and length of the focusing section $4c = 40$ m. The resulting angular acceptance is $\Delta\theta = 1.5°$.

To single out the effect of gravity and to better illustrate that, certain simplifications have been added to the model. Regarding reflector performance, the reflectors are constructed from ideal supermirrors, disregarding changes in supermirror reflectivity as a function of momentum transfer and effects such as absorption. A virtual source is used, with a uniform wavelength distribution extending from 2 to 10 Å, and it is located at the entrance focal point of the *Selene* guide. The size of the source is $1 \times 1\,\text{mm}^2$ and its divergence is adjusted to compensate for the crooked neutron trajectories that might result in some of the long-wavelength neutrons missing the far end of the reflector. As a result, the entirety of the reflecting surface of the first *Selene* element is illuminated by neutrons of all wavelengths.

Figure 6.5 shows the intensity maps at the intermediate focal point P_2, simulated with and without including gravity (bottom and top row, respectively). To single out with which trajectory certain features in the intensity maps are related, the first and second half of the first guide element were interchangeably switched to be vertically absorbing. The horizontal reflection element was fully reflecting in all cases.

The coma aberration, inherent to the elliptical shape of the reflectors, is evident in the intensity maps in the top row. Reflecting on the first half of the vertical elliptical reflector (left image) contributes a broad beam

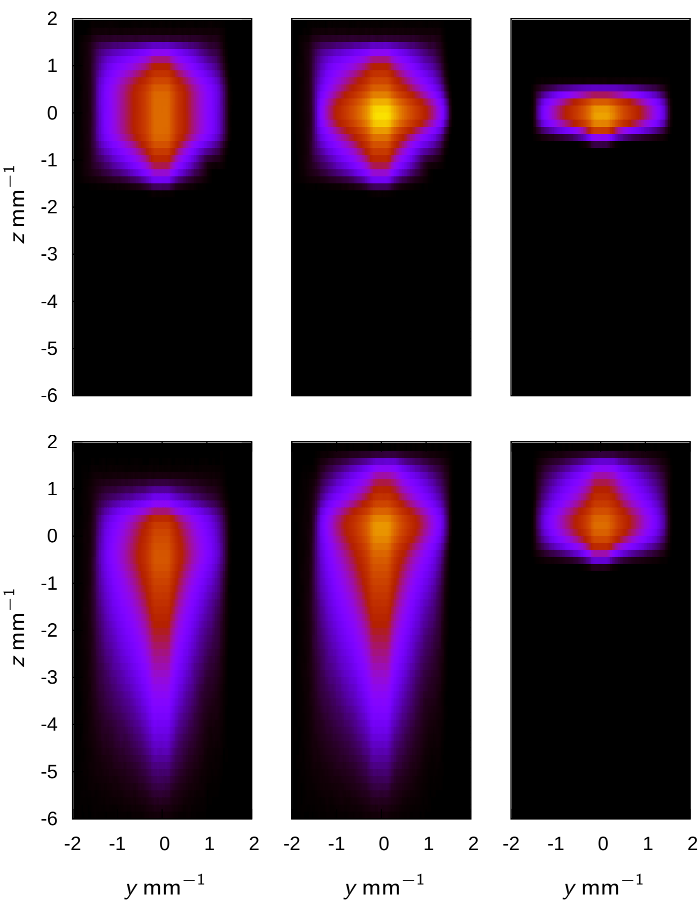

Figure 6.5: Intensity maps $\log_{10}[I(y,z)]$ at the intermediate focal point P_2 of a *Selene* guide system with a total length of 40 m. The upper row was simulated without gravity, the lower one with gravity. For the left/right column only the first/second half of the vertically reflecting guide element was actually reflecting. The middle column was obtained with reflection along the full guide element. The incident slit was $1 \times 1\,\text{mm}^2$, the wavelength range was $\lambda \in [2, 10]$ Å.

profile at P_2. In an inverse manner, reflecting on the second half of the vertical elliptical reflector (right image) results in a highly focused beam profile. As expected, the centre image in the top row, generated by reflecting on the complete first element, shows no difference in the intensity profile between the vertical and horizontal direction.

Gravity is included in the simulations shown in the bottom row. While no change in focusing is observed in the horizontal direction, a tail becomes visible in the vertical direction. Gravity does little to improve the focusing of neutrons reflected on the first half of the vertical elliptical reflector. The vertical tail is also shown to originate almost exclusively from reflections on the first half of the reflector. Reflections on the second half of the vertical elliptical reflector (bottom right image), are found to result in some smearing out of the bright focused spot, along the positive direction of the vertical axis. It was further clarified, through simulations using a single wavelength, that the vertical position of the focusing spot at P_2 shifts upwards, scaling with neutron wavelength. On one hand, the height of the focusing position for longer wavelengths is shifted upwards, and on the other hand, the long-wavelength neutrons are also more heavily influenced by gravity on their way to the second *Selene* element.

The intensity maps of the beam spot at the exit focal point P_3 are shown in figure 6.6, simulated with and without gravity. In the graph to the right, the intensity is integrated along the horizontal direction and the distribution of intensity as a function of the vertical position is shown for selected wavelengths.

Comparing the intensity maps, the beam profile appears to be close to fully restored. It becomes apparent that a compensating mechanism exists for the effect of gravity for small λ, once the neutrons have travelled through and interacted with the full length of the *Selene* guide. The integrated intensity as a function of vertical position indicates that for small wavelengths, e.g., 3 Å, the effect of gravity is negligible. For wavelengths near the upper end of the range that is expected at ESS for a *Selene* type reflectometer, there is an observable change, manifested by a vertical shift of the centre of the focused spot by approximately 0.3 mm, broadening at the base by nearly the same amount and a corresponding reduction in the intensity of the maximum plateau by about 15%.

The $I_\lambda(z)$ graph illustrates that there is only a week chromatic aberration up to at least 6 Å and a moderate effect at 9 Å. Above that the picture changes, the intensity for $\lambda = 15$ Å, for example, is distributed over 4.5 mm with a bimodal distribution. Obviously there is an upper limit for $x^2\,\lambda^2$, up to which the *Selene* guide has low chromatic aberration due to gravity.

In a further set of simulations the geometry shown in figure 6.4 was turned upside down, i.e. the first guide element reflecting downwards and the second upwards. The essential difference is, that for longer wavelengths the intensity is reduced (some 10% at $\lambda = 9$ Å), while the spot size is slightly smaller.

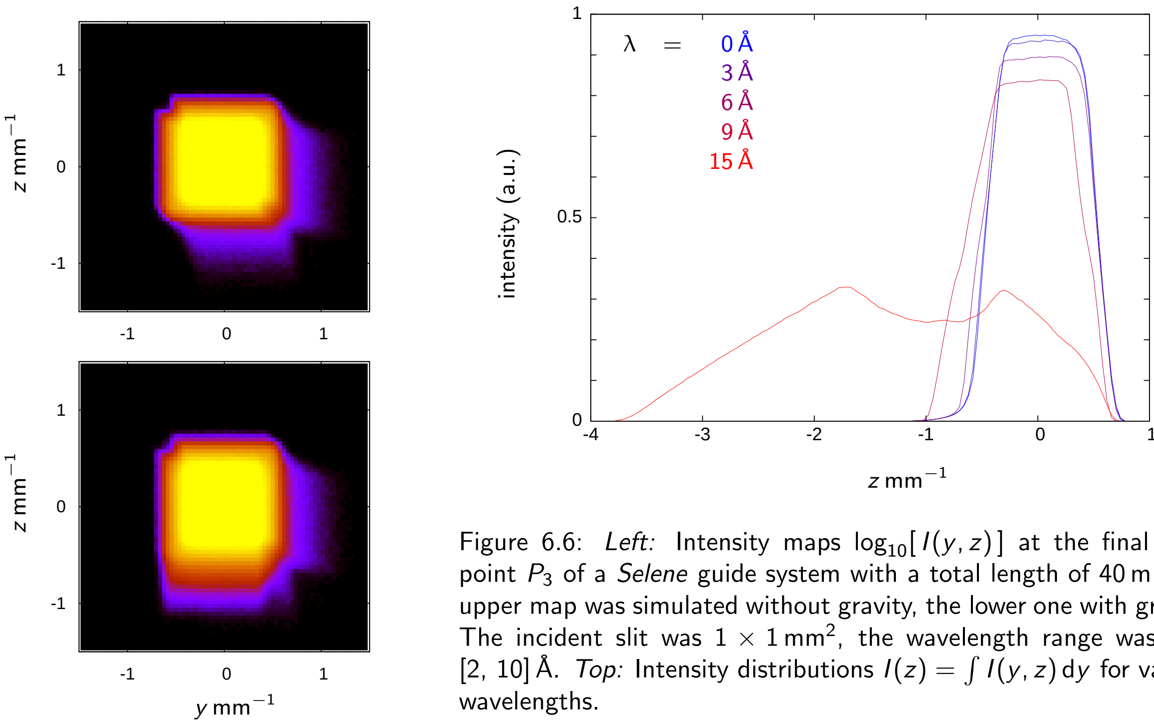

Figure 6.6: *Left:* Intensity maps $\log_{10}[I(y,z)]$ at the final focal point P_3 of a *Selene* guide system with a total length of 40 m. The upper map was simulated without gravity, the lower one with gravity. The incident slit was $1 \times 1\,\text{mm}^2$, the wavelength range was $\lambda \in [2,\,10]$ Å. *Top:* Intensity distributions $I(z) = \int I(y,z)\,\mathrm{d}y$ for various wavelengths.

discussionTaking into account that the actual length of one *Selene* section will be 24 m instead of the 40 m used here, while keeping the λ range, one can assume that the chromatic aberration plays in the sub-mm range for the proposed reflectometer with two *Selene* sections [$\rightarrow$**??**]. In addition, it affects only the spot size normal to the scattering plane.

6.5 transmission

The effective flux at the sample can be estimated by reducing the initial flux $I_0(\lambda)$ by the losses due to reflections on the guide walls. The double *Selene* guide concept involves 8 reflections for all neutrons on surfaces with a non-perfect reflectivity R (plus further reflections in the extraction unit). The angle of incidence on the guide surface hardly varies along the guide for the presented concept: $\theta \approx \epsilon = \Delta\theta/2\xi$,. One can thus assume $R(q_z) = R(\lambda, m)$, with the optimised coating m [$\rightarrow$6.1.9]. This leads to and an attenuation of

$$I(\lambda) \quad = \quad I_0(\lambda) \cdot \prod_{i=1}^{n} R(\lambda, m_i) \tag{6.5.1}$$

n is the number of reflections,. This pushes the flux maximum to higher λ. For the example given in figure **??** a linear decrease of R with λ was chosen:

$$R(\lambda, m) \quad = \quad \begin{cases} 1 & \text{for } \lambda > m\,\lambda_{\text{min}} \\ 0 & \text{for } \lambda < \lambda_{\text{min}} \\ \frac{13}{12} - \frac{1}{12}\,\frac{m\,\lambda_{\text{min}}}{\lambda} & \text{else (i.e. 50\% reflectivity at } m = 7 \text{ and 100\% at } m = 1) \end{cases} \tag{6.5.2}$$

The coating was characterised by $m = 2.5$.

7 Optics and Beam Shaping

7.1 frame-overlap and polarisation filter

For a small source the beam divergence at a point *far* from the source is small, which allows for filtering (polarisation, wavelength) with a transmission filter with convenient coating. The problem is that the filter (surface) has to have a shape $f(x)$ so that it is struck under the same angle γ for any intersecting beam emerging from the source at an angle α. This leads to the conditions

$$\begin{aligned}
\tan\alpha &= \frac{f(x)}{x} \\
f'(x) &= \tan(\alpha+\gamma) \\
&= \frac{\tan\alpha+\tan\gamma}{1-\tan\alpha\,\tan\gamma} \\
&= \frac{\frac{f(x)}{x}+\tan\gamma}{1-\frac{f(x)}{x}\tan\gamma} && (7.1.1) \\
&\approx \frac{f(x)}{x}+\gamma \quad \text{for small } \gamma \text{ and } \alpha && (7.1.2)
\end{aligned}$$

with $f(x)/x$ the slope of the trajectory of the beam. $f'(x)$ is the slope of the surface at the intersection point. It is assumed here that all angles are small. The solution for the simplified differential equation (7.1.2) is

$$f(x) = \gamma\, x \ln\left[\frac{x}{x_h}\right] \qquad (7.1.3)$$

where x_h is a scaling factor given by the intersection of $f(x)$ with the horizon $f(x_h)=0$.
The intersecting point is obtained by

$$\begin{aligned}
\gamma\, x \ln\left[\frac{x}{x_h}\right] &= x\tan\alpha \\
\gamma \ln\left[\frac{x}{x_h}\right] &\approx \alpha \\
x(\alpha) &= x_h \exp\left[\frac{\alpha}{\gamma}\right]
\end{aligned}$$

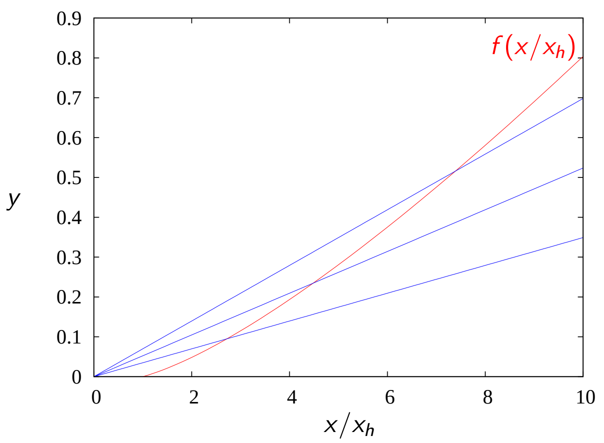

Sketch of the geometry of a surface $f(x)$ which is hit by all trajectories $y = x\tan\alpha\,(\forall\alpha)$ at the same angle γ. Here $\gamma = 2^\circ$ and $\alpha = 2^\circ, 3^\circ, 4^\circ$ are displayed.

Since the problem is centrosymmetric, one can rotate f around the origin (which is the same as changing x_h).

A possible application is the simultaneous use of such a device as frame overlap filter and polariser. For the **low-pass for** λ the ideal coating is Ni with $R = 1$ for $q < q_{\mathrm{Ni}}$. The (idealised) cut-off angle is then given by

$$\sin\gamma = q_{\mathrm{Ni}} \frac{\lambda_{\mathrm{max}}}{4\pi}$$

Below the Ni coating a polarising SM can be deposited with

$$m = 4\pi \frac{\sin\gamma}{\lambda_{\mathrm{min}}\, q_{\mathrm{Ni}}} = \frac{\lambda_{\mathrm{max}}}{\lambda_{\mathrm{min}}}$$

8 Boundary Conditions and Consequences

Based on information distributed at IKON3, and on private communications with P. Bentley, K. Anderson, and H. Wacklin, 11. 2012, there are the following boundary conditions to be expected for a *short* reflectometer. Short means of the order of 50 m long or less, i.e. situated in one of the inner guide halls at the ESS.

8.1 space

- The first 2 m around the moderator are free of any elements.
- Within the target monolith shielding (2 to 6 m) an insert of horizontally a 5° wedge, but less that 210 mm, and vertically of 210 mm can be freely shaped. Optical elements are allowed in the insert. Since there will be a cooled He atmosphere (from moderator up to the end of the monolith) also free-standing Si-wavers can be used.

  The last 500 mm of the monolith might be occupied by a shutter (which can host optical elements).
- Behind the monolith there might be a chopper or other moving parts.
- From the monolith up to a radius of 15 m a common shielding for all instruments will be build. The beam guide can be of any shape and size. There is the option to insert choppers and other devices (most likely accessible from top).
- At a distance larger than 15 m to the moderator, the individual instrument guide shielding starts. Its length depends on the dose rate caused mainly by fast neutrons (also by secondary processes).
- The *short* instruments will have a 10° wedge-shaped space available. This is necessary to allow for sufficient shielding to prevent cross-talk of background.
- The height differences from moderator to floor are 3 m and 2 m. The hall allowing for high magnetic fields will have the 2 m distance. If needed it is possible to get a lower floor locally.

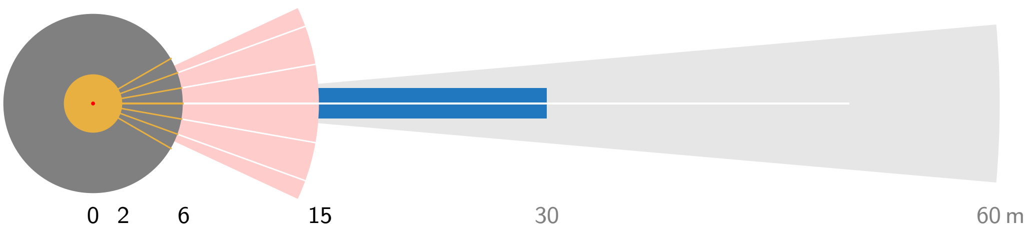

Figure 8.1: Sketch to illustrate the various shielding jackets intended for the source and the instrument. The colours mean: red–moderator, yellow–He-atmosphere, gray–target-shielding, light red–common instrument shielding, blue–individual guide-shielding (as far as possible), light gray–10° wedge available for a short instrument.

8.2 shielding and background

- The target monolith (for the moment) is intended to consist of steel.
- The common instrument shielding will be made of various materials to moderate fast neutrons, convert muons and neutrons, and absorb γ and neutrons.
- The effective direct line of sight from any point of the instrument area to the moderator and target is to be avoided. This means at least 12 m material in the direct line.

  At most half of the length of the guide (shielding) is to have direct line of sight.
- Indirect line of sight has to be avoided. I.e. from outside the shielding no area directly illuminated by the source (moderator and target) is visible. Here the thickness of the shielding material is about 2 m?

U. Filges made MCNPX calculations for a reference shielding, which does not fulfil the mentioned criteria. It is made of steel, only, and allows for a direct line of sight from sample (detector) to the moderator. !!!

Based on these constrains it might be favourable to substitute the one *Selene* guide section as discussed in section **??** for two identical sections of half the lengths. Direct line of sight is blocked much earlier and the joining focal point is in an environment of low radiation allowing for easy access. The two versions are discussed in sections **??** and **??**.

8.3 exclusion of proton prompt

At ISIS second target station and at the SNS the fast neutrons and hard x-rays produced during the proton pulses (or by secondary processes in the shielding) cause problems in the data acquisition. The corresponding STAP members R. Dalgliesh and J. Ankner suggest not to collect data during these times. So it is favourable to tune the instrument length and λ-range in a way to exclude the pulse times without creating holes in the q-range.

For the time being all reflectometers should be developed in a way that the time interval of high fast neutron background is excluded from the measurements.

Following the argumentation of section **??** the usable wavelength range for reflectometry starts at about 4 Å to 5 Å for *Selene* guides. An instrument length of some 60 m results in a wavelength range of e.g. $\lambda \in [5, 10]$ Å. For the ESS baseline parameters this has the consequence that the background burst from the proton pulse appears at the be beginning or the end of the used wavelength range. Further optimisation leads to the situation that the bursts are just outside the required λ range, as is sketched in figure 8.2.

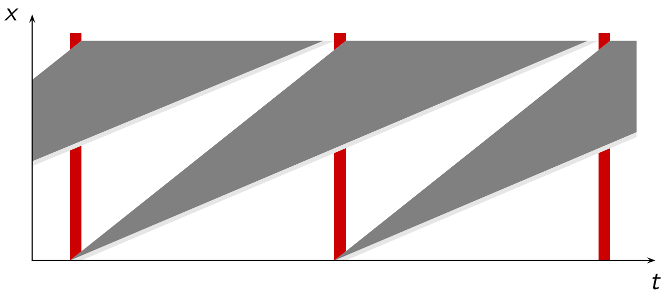

Figure 8.2: Sketch to illustrate how to avoid the influence of the γ and fast neutron burst from the proton pulse hitting the target. The sketch is to scale with period $T = 70$ ms, pulse length $t = 3$ ms, and a sample detector distance of 58 m, i.e. $\lambda \in [5, 9.3]$ Å.

For this scheme, the flight times for the shortest / longest wavelength are $t = 73$ ms / 137 ms (assuming a burst time of 3 ms and a period of 70 ms). For $\lambda_{\mathrm{min}} = 5.00$ Å this leads to an instrument length of $\overline{SD} = 58'400$ mm, and this in turn to $\lambda_{\mathrm{max}} = 9.38$ Å.

8.3.1 intrinsic resolution

The intrinsic λ resolution for this instrument is given by the length of the flight path X, and the pulse length τ via

$$\begin{aligned}
\frac{\Delta\lambda}{\lambda} &= \frac{\Delta t}{t} \\
&= \frac{\tau}{2.53 \cdot 10^{-4}\,\mathrm{s\,m^{-2}}\,X\,\lambda} \\
\Delta\lambda &= 3\,956\,\mathrm{m^2\,s^{-1}}\,\frac{\tau}{X} \\
&\approx 0.2\,\text{Å} \qquad \text{for } X = 58.4\,\mathrm{m},\ \tau = 2.85\,\mathrm{ms}
\end{aligned}$$

This leads to

$$\frac{\Delta\lambda}{\lambda} \quad = \quad 4.0\% \ldots 2.1\% \quad \text{for} \quad \lambda = 5\,\text{Å} \ldots 9.4\,\text{Å}.$$

9 Technical Details

9.1 moving elements

This section gives a preliminary list of translation and rotation stages, sorted by location and purpose. All motion devices besides the guide positioning and alignment are also listed in table **??** with estimated ranges, accuracy, and load.

9.2 detector characteristics

According to Richard Hall-Wilton, ESS, it is realistic to expect the following parameters:

resolution:	$0.5 \times 0.5\,\mathrm{mm}^2$	minimum
size:	$500 \times 500\,\mathrm{mm}^2$	maximum

	motion	range	accuracy	load	moment
apertures within ellipses	y translation	$0 - 80$ mm	< 1 mm	20 kg	
	z translation	$0 - 80$ mm	< 1 mm	20 kg	
	y translation	$0 - 80$ mm	< 0.1 mm	2.0 kg	
	z translation	$0 - 80$ mm	< 0.1 mm	2.0 kg	
beam definition	x translation	$0 \ldots 40$ mm	< 0.1 mm	2 kg	
	z translation	± 20 mm	< 0.1 mm	5 kg	
	tilt	$\pm 5°$	$< 0.01°$	10 kg	
	roll	$\pm 5°$	$< 0.01°$	15 kg	
	x translation	± 20 mm	< 0.01 mm	20 kg	
	y translation	± 20 mm	< 0.01 mm	25 kg	
	ω	$0° \ldots 360°$	$< 0.002°$	30 kg	
	2θ	$\pm 2°$	$< 0.01°$		10^6 Nm
	x translation	± 100 mm	< 0.1 mm	0.5 t	
	y translation	± 100 mm	< 0.1 mm	0.5 t	
fast aperture	y^+ translation	$0 \ldots 80$ mm	< 0.01 mm	1.0 kg	
	y^- translation	$0 \ldots 80$ mm	< 0.01 mm	1.0 kg	
	z^+ translation	$0 \ldots 80$ mm	< 0.1 mm	1.0 kg	
	z^- translation	$0 \ldots 80$ mm	< 0.1 mm	1.0 kg	
sample stage	z translation	± 20 mm	< 0.1 mm	0.6 t	
	tilt	$\pm 5°$	$< 0.01°$	0.7 t	
	roll	$\pm 5°$	$< 0.01°$	0.7 t	
	x translation	± 20 mm	< 0.01 mm	0.8 t	
	y translation	± 20 mm	< 0.01 mm	0.8 t	
	ω	$0° \ldots 360°$	$< 0.002°$	1.0 t	
	2θ	$-5° \ldots 140°$	$< 0.01°$		$2 \cdot 10^5$ Nm
	x translation	± 500 mm	< 0.1 mm	1.5 t	
	y translation	± 500 mm	< 0.1 mm	1.5 t	
CCD camera	z translation	$0 \ldots 400$ mm	$^\dagger < 0.01$ mm	10 kg	

Table 9.1: Parameters for motion control, sorted by locations and purpose., For beam manipulation and sample stage a classical set-up using rotation and translation stages was assumed. † only end-position.

As consequence the highest resolution at $q = 0.01\,\text{Å}^{-1}$ with a sample-detector distance of 6.2 m, limited by the detector is

$$\begin{aligned}
\Delta\theta &= \arctan[0.5/6200] \\
&\approx 0.005^\circ \\
\theta &= 0.43^\circ \quad \text{for } \lambda_{\max} = 9.4\,\text{Å} \\
\Delta\theta/\theta &= 1.1\%
\end{aligned}$$

Since the length of the flight path is optimised to avoid the proton pulse time it is not advisable to change the sample-detector distance. So it could be mounted on a 2θ arm of fixed length, with a evacuated, frustum-shaped nozzle pointing towards the sample.

sizeA width of 500 mm results in an angle range of 4.6°. This is three times the maximum divergence of the beam incident on the sample. The excess area in the scattering plane is needed for off-specular measurements: When using λ-θ encoding, the specular beam scans over the inner 1.5°, so that effectively only another $\pm 1.5^\circ$ are available.

Normal to the scattering plane the maximum area of interest is 170 mm wide, only. So the expected minimum detector size is

$$\begin{aligned}
\text{width} \quad y &= 500\,\text{mm} \\
\text{height} \quad z &= 170\,\text{mm}
\end{aligned}$$

resolutionIn the scattering direction (i.e. horizontally) a high resolution is required. Ideal would be a pixel-size of 0.5 mm or less. The lower limit is given by the effective sample size of a fraction of a mm.

Normal to the scattering plane (vertical) a much coarser resolution can be accepted. In an ideal case no position sensitivity is needed at all. A real effect that might still require some resolution are the suppression of background *outside* the region of interest. And also to align the *roll* of the sample (tilt around the x-axis) a 2-dimensional detector would be favourable. But this task could also be performed with an optional CCD-camera.

$$\begin{aligned}
\text{horizontal} \quad \Delta y &\leq 0.5\,\text{mm} \\
\text{vertical} \quad \Delta z &\in [\Delta y, \infty]
\end{aligned}$$

rate per pixel Since the pixel size is not defined, here the maximum rate per mm^2 is given. It was obtained by assuming a perfectly reflecting reference sample of $10 \times 10\,\text{mm}^2$ and full beam divergence (i.e. the reference for normalisation as discussed in section **??**). The rate per pixel varies in the range

$$\begin{aligned}
10^5\,\text{s}^{-1}\text{Å}^{-1}\text{mm}^{-1} \quad &\text{for} \quad \lambda = 5\,\text{Å} \\
3 \cdot 10^4\,\text{s}^{-1}\text{Å}^{-1}\text{mm}^{-1} \quad &\text{for} \quad \lambda = 9.4\,\text{Å}
\end{aligned}$$

total rate This quantity was obtained by simulation with the same setting as mentioned above, but by integrating over the full detector. The maximum specularly illuminated area is $2.7 \cdot 10^4\,\text{mm}^2$, but the illumination is not homogeneous. The maximum integral rates are

$$\begin{aligned}
5 \cdot 10^8\,\text{s}^{-1}\text{Å}^{-1} \quad &\text{for} \quad \lambda = 5\,\text{Å} \\
2 \cdot 10^8\,\text{s}^{-1}\text{Å}^{-1} \quad &\text{for} \quad \lambda = 9.4\,\text{Å}
\end{aligned}$$

homogeneityThe detector images are normalised by division by a reference measurement. Already a relative mis-alignment of 0.005° leads to a shift of one (0.5 mm) pixel. It is thus crucial that the detector area is homogeneous (if necessary after pixel-wise normalisation) on the order of 1%.

stabilityThe intended measurement scheme requires a reference for each detector image obtained with a sample. To save measurement time, there will be a set of reference sample sizes and orientations available, obtained with standard samples. This requires that the homogeneity of the detector does not change with time (over months), and that the total sensitivity can be detected continuously, so that a renormalisation of the reference is possible.

dynamic range The dynamic range of the detector must be quite high since at the same time one can expect maximum flux on some area of the detector, while it drops by 6 orders of magnitude (or more) for high-q_z or off-specular regions. This can be seen in figures **??** and **??**.

A signal of 10^{-8} relative to the full intensity given by a *small* sample should be measurable. Small here means 2 orders of magnitude smaller than the reference mentioned above. The signal will then be of the order $5 \cdot 10^8 \times 10^{-2}\, 10^{-8}$. Thus the integral noise of the detector should be below $10^{-2}\,\mathrm{s}^{-1}$.

10 Measurement Schemes and Data Reduction

This chapter is in a fragmentary state. The samples are not yet completely defined (suggestions are welcome!) — and thus there are no definite simulations.

The process of data acquisition and processing described below is based on experience with measurements using the prototype set-up on BOA and on Amor, both at PSI. Where these are not available, the description states what is intended to be done.

This chapter gives a more detailed description of the data collection and processing for the three principle operation modes and three types of samples.

[→10.1] An organic film at the Si/D_2O interface in a solid/liquid cell, measured in the almost conventional mode.

[→10.2] A NiTi multilayer with (artificial) off-specular scattering, measured with λ-θ encoding.

[→10.3] A small ferromagnetic sample, measured in the high-intensity specular mode.

10.1 conventional mode, solid-liquid cell

Liquid samples typically show a high diffuse scattering. This means that one has to choose an operation mode where diffuse scattering does not strongly affect the specular signal, and where it can be measured to some extend to allow for correction. This is why the combination liquid cell / almost conventional mode is chosen, here.

Measurements using a sold-liquid cell imply the constraint that the footprint has to avoid the sealing regions of the cell.

10.1.1 the sample

The sample is an organic film on Si, measured against D_2O/H_2O.

Si	∞	SLD
SiO_2	20 Å	
σ	2 Å	
film	50 Å	
σ	2 Å	
D_2O/H_2O (9:1)	0.2 mm	

The incoherent scattering from H in film and solvent is taken into account.

10.1.2 the measurement scheme

This mode corresponds to the conventional TOF reflectometry, where the beam divergence and footprint size are defined by slits. The angle of incidence and the divergence are constant over the pulse. Using the *Selene* guide the footprint defined by the slit system at the virtual source point. For adjusting the divergence one slit behind the last guide element is sufficient. The still convergent beam avoids illumination of the sample environment.

Due to the analogy, the data collection, normalisation and further treatment for one angle of incidence exactly follow the procedure used with conventional TOF reflectometers.

An additional feature when using a wide divergence cut down by the slit is, that by scanning the slit in between measurements, one can change θ without rotating the sample.

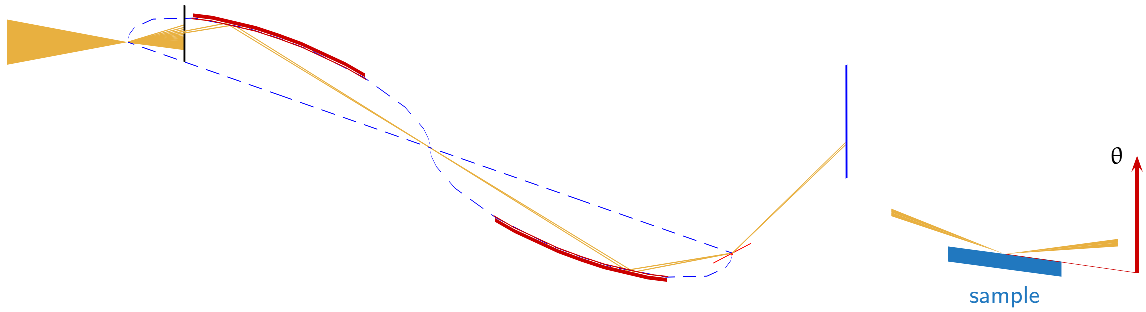

10.1.3 sample alignment

. The low-divergent beam caused by the slit allows to align the sample by alternating rocking scans and z-scans. The accuracy is given by the divergence and for larger samples by the footprint. The only difference to conventional TOF reflectometers is that the beam converging at the centre of rotation should not have any parallel components. A z scan at $2\theta = 0°$ to find the absorbing substrate at the half-shaded beam is thus modified. At $\theta = 0°$ one has the end of the substrate leading to half the intensity, and not the sample centre. For small samples this can be neglected, for large samples one still gets the approximate position.

For a high precision of the alignment an additional CCD-based detector can be used. It has much higher resolution and fast feed-back (no TOF analysis is necessary).

One can use divergent white light coupled into the beam before the virtual source point. Besides gravity effects this follows the same trajectories as the neutrons, creating a spot where the centre of rotation should be. Depending on the (transparency of) the sample environment one can thus use the light to pre-align the sample. This method is used on Amor and on the *Selene* prototype with large success.

10.1.4 data acquisition

For the ... sample measured through Si the critical edge is at $q_z^c = ?\,\text{Å}^{-1}$. This leads to the lowest angular setting $\omega = ?°$. The corresponding q_z range, slit-opening (centred in the middle of the beam), and counting times are given in table 10.1.

ω	$q_z/\,\text{Å}^{-1}$	$s/\,\text{mm}$	$t/\,\text{s}$

Table 10.1: Angular settings ω, the related q_z range, the slit-width s, and the estimated counting time t.

The criterion for the counting time is that the highest statistical error per $\Delta q/q = 4\%$ bin is below ?%.

The measurements each lead to an array $I(y, z, t)$. In most cases (as here), there is no information expected in y direction so that one can project the array to $I(z, t)$. The uncertainties are Δz given by the detector resolution, and $\Delta t = \tau$.

10.1.5 reference measurement

The best normalisation can be obtained using a reference sample cell, where the film (and solvent) are replaced by a supermirror coating of known reflectivity. It is realistic to assume a $m = 10$ coating with a moderate reflectivity.

So for up to $q_z = 0.22\,\text{Å}^{-1}$ one gets the reference arrays $I_r(y, z, t)$ or $I_r(z, t)$. Correction for the known reflectivity gives $I_{rc}(z, t)$.

10.1.6 normalisation and integration

If required, the not specularely illuminated area of the $I(z, t)$ map can be used to estimate the diffuse background, which can then be subtracted from $I(z, t)$.

A division of $I(z, t)$ by the reference $I_{rc}(z, t)$ pixel-by-pixel gives the reflectivity of the film $R(z, t)$. This can be transferred to $R(q_x, q_z)$, or if the off-specular region can be ignored, the corresponding region of $R(z, t)$ can be projected on a q_z grid with $\Delta q_z/q_z = \text{const}$. The new q_z grid should have a lower resolution compared to $R(z, t)$, which is defined by the detector resolution Δz and by τ. Here $\Delta q_z/q_z = 7\%$ is used.

10.1.7 discussion

...

A limiting factor for using the proposed instrument for solid-liquid-cells is the maximum footprint of $10 \times 40\,\mathrm{mm}^2$. Larger samples will profit from an other geometry, or from a non-focusing instrument.

Within these limitations the intensities and measurement times should be almost the same on all reflectometer types, because the maximum intensity (as allowed by Liouville) is reduced by the guide transmission, only.

The diffuse background scales roughly as $A^2 \times \Delta\theta_y^2 \times \Delta\theta_z^2$, ($A$ is the sample surface) while the specular intensity scales with $A \times \Delta\theta_y \times \Delta\theta_z$. It is thus possible to increase the signal-to-background ratio by reducing any of these quantities. It has to be analysed how far this can be taken — or if the small sample surface can be compensated for by using a higher divergence.

10.2 λ-θ encoding, off-specular measurements

The strengths of the λ-θ-encoding are the wider q_z range accessible with one angular setting, the constant $\Delta\lambda/\lambda$, and eventually the *nicer* off-specular area, compared to the almost conventional mode.

This is illustrated at the example of a Ni/Ti multilayer sample with (artificial) Bragg-sheet scattering.

The high resolution $\Delta q_z/q_z = 2\%$ aimed for *here* results in much longer counting times.

10.2.1 the sample

The sample is a multilayer of the composition

$$[\,\mathrm{Ni}\,(?\,\text{Å})\,/\,\mathrm{Ti}\,(?\,\text{Å})\,]_?/\mathrm{Si}$$

with a constant interface roughness $\sigma = 4\,$Å. The off-specular signal is *generated* using the specular reflectivity $R(q_z)$

$$R(q_x, q_z) \quad = \quad R(q_z) \cdot \exp\left[-\frac{q_x^2}{2?^2}\right]$$

with a cut-off at the sample horizon. A bending of the Bragg sheets, Youneda wings and the low-intensity region between Youneda and horizon are not produced this way. Within McStas this folding is achieved by randomly adding a q_{xy} component, but with a Gaussian probability distribution centred at $q_{xy} = 0$.

10.2.2 the measurement scheme

A ML monochromator at or before the virtual source point encodes the wavelengths of the neutrons in the final angle of the monochromator. For small θ one gets $\theta \propto \lambda$. The specular reflectivity from the sample then leads to a diagonal streak in $I(\lambda, 2\theta)$ on the detector, so that off-specular scattering can be measured. Figure 10.1 shows *snap-shots* of the beam-distribution within the guide an at the sample.

The resolution in q_z is essentially given by the ML monochromator and can reach 2%, while the TOF resolution influences Δq_x (this has to be verified). So this mode could be realised without any chopper. The losses one gets by using a monochromator are (partly) compensated by the quasi-simultaneous measurement on a wide θ-range.

For a ML with a Bragg peak at $m \cdot 0.022\,\text{Å}^{-1}$ one gets the proportionality (with $[\theta] = \deg$)

$$\theta \approx 0.1\, m\, \lambda / \text{Å} \tag{10.2.1}$$

The guide geometry, its coating and the wavelength range define $\Delta\theta$ [→**??**]. I.e. for $\lambda \in [5, 9.4]\,$Å and $\Delta\theta = 1.5°$ one gets $m \approx 3.4$ with $\theta \in [1.7°, 3.2°]$. A plateau of total reflection ($m \leq 1$) results in $\theta \leq 1°$ for the same λ range. Thus totally reflected neutrons do not reach the guide.

fast moving slit A ML monochromator leads to an illumination of the *off-specular region* on the detector by diffuse and and off-specular scattering at the multilayer, but also by specular scattering off the Bragg condition!. This can be seen in figure 2.7. A fast moving slit before the sample can be used to filter this unwanted intensity from the monochromator. The slit scans across the beam for each pulse and thus also creates a λ-θ encoding, but without the constant resolution. In combination with the monochromator the slit keeps the off-specular region clean.

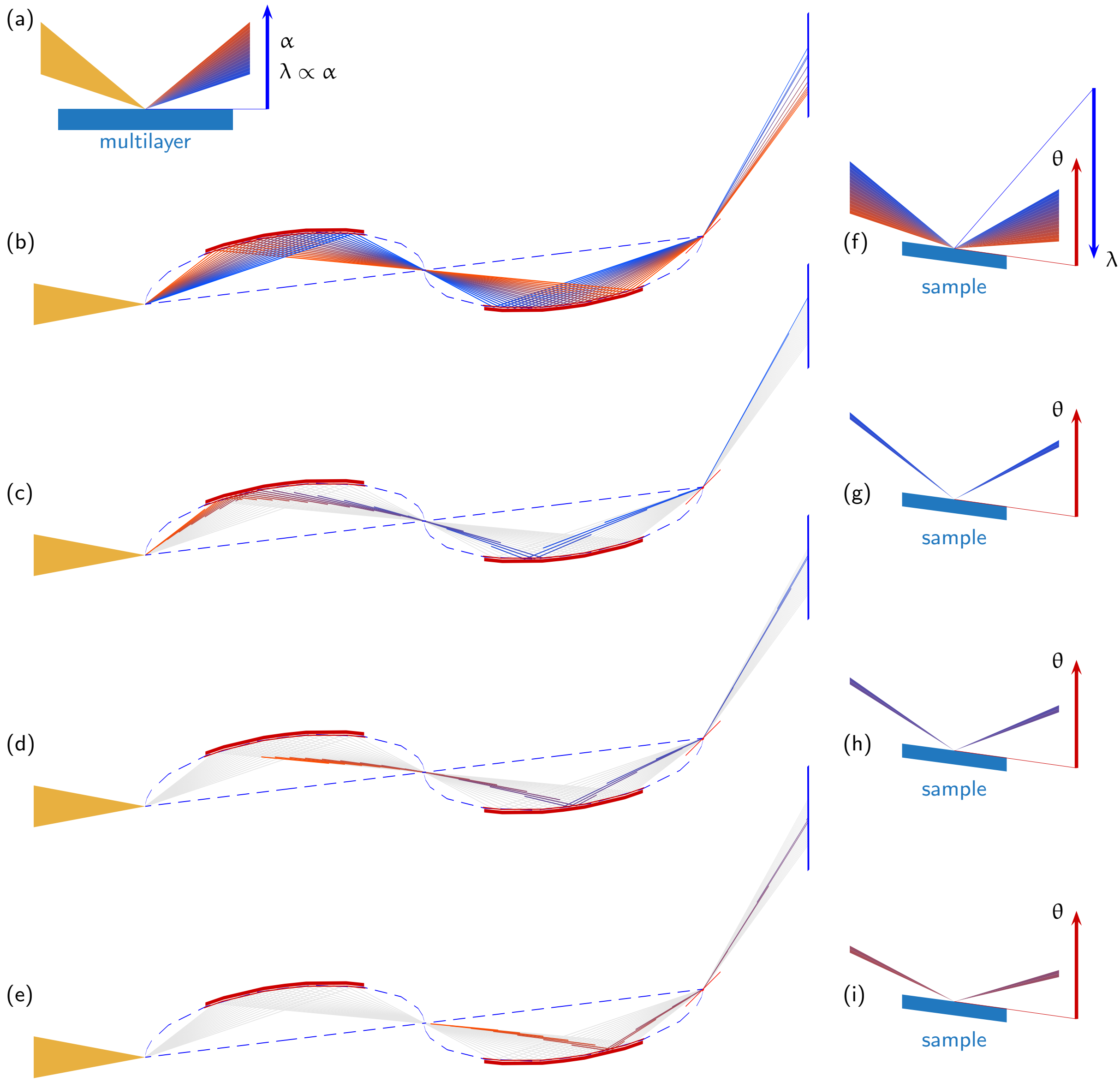

Figure 10.1: Illustration of the principle of the λ-θ encoding. A convergent white (pulsed) beam is spectrally analysed by a ML monochromator (a). The beam then propagates to the sample keeping the relation between λ and θ (b). For a pulsed beam at any time an almost monochromatic beam is impinging on the sample, where θ and $\lambda \sim \theta$ vary with time. The sketches (c) to (e) show snap-shots of the beam within the *Selene* guide system and after the sample. In (f) to (i) the corresponding situation on the sample is shown.

10.2.3 sample alignment

The sample can be aligned by keeping the otherwise scanning slit behind the guide at a fixed position with small opening. The beam transmitted there is then well-defined, but almost monochromatic. The further procedure follows the one described above [→10.1.3].

10.2.4 data acquisition

Also the data acquisition follows the scheme of the almost conventional reflectometry. Only the number of q_z-ranges is reduced, and the counting times are increased.

table

10.2.5 reference measurement

For $q_z < 0.2\,\text{Å}^{-1}$ a high-m supermirror with known reflectivity and same shape as the sample can be used for normalisation. For higher q_z it is possible to correct the reference measurements for the footprint size. To avoid problems with detector inhomogeneities, the same detector area should be illuminated for all measurements.

10.2.6 normalisation and integration

The normalisation here is a bit more complicated because there is no reference sample with a well-known high-intensity off-specular scattering.

...

10.2.7 discussion

...

It is not yet clear if a fast slit system is available. In the worst case one could use a pair of choppers for this purpose, but they would be located quite close to the sample.

10.3 high-intensity specular mode, small magnetic sample

10.3.1 the sample

10.3.2 the measurement scheme

Figure 10.2: text !!!

Measurements performed on Amor with one guide, only, are shown in figure 10.3

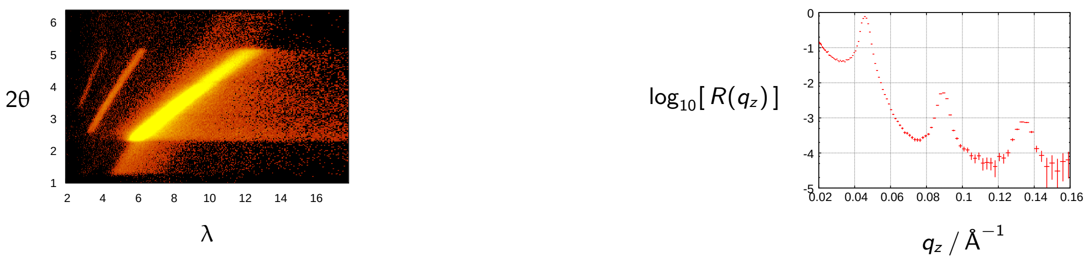

Figure 10.3: text

10.3.3 sample alignment

The sample can be aligned by using the slit behind the guide at a fixed position with small opening. This is identical to the situation in the almost conventional mode and thus the scheme described there can be used [→10.1.3].

10.3.4 data acquisition

10.3.5 reference measurement

To normalise the $I(t, y, z)$ data set the best choice is to use a reference sample with the same measures (to guarantee the same footprint) and a high reflectivity over a wide q_z range. As long as $R_r(q_z)$ of this reference is known, one can correct the reference $I_r(t, y, z)$ to $I_{rc}(t, y, z) = I_r(t, y, z)/R_r(t, y, z)$.

One can think of using a supermirror with $m = 10$, and reflectivity $R > 1\%$ as a reference. This would allow direct corrections up to $q_z = 0.22\,\text{Å}^{-1}$. Since each reference measurement takes some time, a set of standard sample sizes should be defined, for which the corresponding reference measurements are available. This applies also to liquid-solid cells.

10.3.6 normalisation and integration

In case a reference reference measurement is available (i.e. $q_z \approx 0.22\,\text{Å}^{-1}$) it s possible to normalise the measurement pixel-by-pixel to get

$$R(t,y,z) \quad = \quad I(t,y,z)/I_{\rm rc}(t,y,z) \tag{10.3.1}$$

Summation over y, transformation of t to λ with $\Delta t = \tau$, and z to 2θ with the detector resolution Δz gives a $R(\lambda,\theta)$ map with corresponding error-map. Each line (one θ) corresponds to a reflectivity $R_\theta(\lambda)$ obtained in TOF mode, and each column (one λ) corresponds to a reflectivity $R_\lambda(\theta)$ obtained in an angle-dispersive mode.

There are various schemes to collapse the $R(\lambda,\theta)$ to $R(q_z)$. The approach we followed up to now is the define a q_z grid (with $\Delta q_z/q_z =$ constant) and to fill in all entries of the $R(\lambda,\theta)$ array according to their q_z. This can be done with full error handling so that at the end each $R(q_z,i)$ has its own error. Since the resolution varies over the $R(\lambda,\theta)$ array, one gets a non-trivial but known resolution function for $R(q_z)$.

For higher q_z, where no reference is available, or its measurement would take too long, it proved to be possible to take a low-ω measurement and eventually correct for the different footprint or projected sample height. In case the detector is not sufficiently homogeneous, one has to take care to illuminate the same area on the detector for all ω.

10.3.7 discussion

10.4 data reduction

10.4.1 raw-data and intensity maps

Each neutron detected on the position sensitive detector has the associated parameters t, y and z for the time-of-flight and the position on the detector. The detector spatial resolution gives the constant values Δy and Δz, the pulse length sets an upper limit for $\Delta t <= \tau$. The latter one might be reduced by choppers.

From theses basic parameters and the instrument parameters X (source detector distance) and $\theta_{\rm detector}$ one can calculate the neutron wavelength [→**??**]

$$\lambda \quad = \quad \frac{h}{m_{\rm n}}\frac{t}{X} \tag{10.4.1}$$

and the final angle after reflection

$$\theta_{\rm f} \quad = \quad \hat{\theta} + \omega - \arctan z \tag{10.4.2}$$

where ω is the inclination of the sample surface relative to the long axis of the last ellipse of the *Selene* guide, z is the position on the detector if that one is located at $\theta_{\rm detector} = \hat{\theta} + 2\omega$.

Discretisation in λ and $\theta_{\rm f}$ of a large ensemble of events gives the intensity map $I(\lambda,\theta_{\rm f})$ with the error-map $E(\lambda,\theta_{\rm f}) \approx \sqrt{I(\lambda,\theta_{\rm f})}$. The approximation is valid for more than 10 counts per bin. For less counts a correcting factor has to be taken into account. Zero counts is also a measured quantity and has to have an error. This topic has to be investigated further!

It is also possible to extract $I(q_z)$, $E(q_z)$ or $I(q_z,q_x)$, $E(q_z,q_x)$, instead. ...

10.4.2 normalisation

The measured intensity map $I(\lambda,\theta)$ is not only a function of $R(q_z)$ of the sample, but also of the intensity $I_{\rm sample\ in}(\lambda,\theta,x,y)$. incident on it. This quantity could ideally be measured with a reference sample with $R(q) = 1$ and exactly the same shape and position as the sample. Non-perfect reflectivity can be corrected for as long as $R_{\rm reference}(q)$ is known and homogeneous. One could e.g. use a supermirror-coated reference with $m = 10$ (and low reflectivity) to correct up to $q_z = 0.22\,\text{Å}^{-1}$.

For higher q_z this approach is unrealistic. On the other side the projected sample height is larger, which leads to an averaging over beam inhomogeneities. So it might be possible to use a calculated or simulated reference. The quality of the calculation or simulation can be checked by comparison to the reference below $q_z = 0.22\,\text{Å}^{-1}$.

integration normal to the scattering plane The normalisation can be performed after integrating in y direction on the detector, i.e. normal to the scattering plane. This is justified by

$$
\begin{aligned}
I(t,y,z) &= I(t,z)\cdot g(y) \\
\frac{\int I(t,y,z)\,\mathrm{d}y}{\int I_0(t,y,z)\,\mathrm{d}y} &= \frac{\int I(t,z)\,g(y)\,\mathrm{d}y}{\int I_0(t,z)\,g(y)\,\mathrm{d}y} \\
&= \frac{I(t,z)\,\int g(y)\,\mathrm{d}y}{I_0(t,z)\,\int g(y)\,\mathrm{d}y} \\
&= R(t,z)
\end{aligned}
$$

where $g(y)$ gives the intensity distribution in y direction. By using a single detector or a 1D position sensitive detector this integration is already realised. This is the case in many conventional reflectometers.

10.4.3 resolution

In most cases the resolution function $f(q_z)$ with $R_e(q_z) = R(q_z)*f(q_z)$ will neither be constant nor proportional to q_z. It is thus dangerous to add several data sets, e.g. obtained with various ω.

10.4.4 summation of data sets with different resolution

The summation of data sets $R_i(q_z)$ with different resolution $f_i(q_z)$ is possible, but it leads to a complicated (i.e. not single-Gaussian) resolution function:

$$
\begin{aligned}
R_\Sigma &= \sum_i a_i R_i \quad , \quad \sum_i a_i = 1 \\
&= \sum_i a_i R * f_i \\
\mathcal{F}[R_\Sigma] &= \mathcal{F}\left[\sum_i a_i R * f_i\right] \\
&= \sum_i a_i \mathcal{F}[R * f_i] \\
&= \sum_i a_i \mathcal{F}[R]\cdot\mathcal{F}[f_i] \\
&= \mathcal{F}[R]\cdot\sum_i (a_i\mathcal{F}[f_i]) \\
&= \mathcal{F}[R]\cdot\mathcal{F}\left[\sum_i a_i f_i\right] \\
&= \mathcal{F}\left[R * \left(\sum_i a_i f_i\right)\right] \\
R_\Sigma &= R * \left(\sum_i a_i f_i\right) \\
&:= R * f_\Sigma
\end{aligned}
$$

Simulation or fitting of $R(q_z)$ is possible when $f_\Sigma(q_z)$ can be estimated, and when is taken into account in the simulation software.

For publication such a reflectivity profile might not be suited because the abrupt changes in $f_\Sigma(q_z)$ at the joints can lead to peaks or dips in R_Σ.

10.4.5 convolution to $\Delta q/q = \mathrm{const}$

In cases when the experimental resolution function $f_e(q)$ of one data set $R_e(q) = R(q) * f_e(q)$ is known, one can convolve $R_e(q)$ with a resolution $f_c(q)$ in a way to get $R_p(q)$ with $\sigma_p \propto q$, i.e. $\Delta q/q = \mathrm{const} := p$. For Gaussian the relation

$$
\begin{aligned}
f_{e/c}(q) &= \frac{1}{\sqrt{2\pi}\,\sigma_{f/c}} \exp\left[-\frac{(q-q_{f/c})^2}{2\sigma_{f/c}^2}\right] \\
f_p(q) &= f_e(q) * g_c(q) \\
&= \frac{1}{\sqrt{2\pi}\,\sigma_p} \exp\left[-\frac{(q-q_p)^2}{2\sigma_p^2}\right] \qquad \text{with} \quad \sigma_p^2 = \sigma_e^2 + \sigma_c^2, \quad q_p = q_e + q_c \qquad (10.4.3)
\end{aligned}
$$

holds. For the present case $q_{e/c} = 0$. So when $\sigma^e(q)$ is known one can get the *correcting Gaussian* with

$$\sigma_c(q) = \sqrt{p^2\,q^2 - \sigma_e^2(q)} \qquad (10.4.4)$$

with $\sigma_p = p\,q$. Avoiding $\sigma_c <= 0$ leads to the constraint

$$p > \frac{\sigma_e(q)}{q} \quad \forall q$$

The resulting *corrected* reflectivity curve is then

$$
\begin{aligned}
R_p(q) &= R_e(q) * f_c(q) \\
&= \int_{\bar{q}=q_{\min}}^{q_{\max}} R_e(q-\bar{q}) \cdot \frac{1}{\sqrt{2\pi}\,\sigma_c(\bar{q})} \exp\left[-\frac{\bar{q}^2}{2\sigma_c(\bar{q})^2}\right] \mathrm{d}\bar{q} \qquad (10.4.5)
\end{aligned}
$$

This now allows to merge several data sets after bringing them the the same resolution for each q in the overlapping region. Of cause information is lost by lowering the resolution, but the resulting $R_e(q)$ and eventually a merged $R_\sigma(q)$ have the appearance expected by standard software, most of the users, and almost all readers of publications.

!!! Besides the resolution of the data imposed by the experiment and the data analysis, there is the resolution of the representation of the data, I.e. the spacing of the nodes. To be able to distinguish peaks in $R(q_z)$, already convoluted with the final resolution function $f(q)$, one has to .....

From δq (FWHM) to σ:

$$
\begin{aligned}
\exp\left[\frac{q_{1/2}^2}{2\sigma^2}\right] &= 0.5 && (10.4.6) \\
q_{1/2} &= \sqrt{2\ln 2}\sigma && (10.4.7) \\
\Delta q &= 2\,q_{1/2} && (10.4.8) \\
&\approx 2.3548\,\sigma && (10.4.9)
\end{aligned}
$$

off-specular and incoherent scattering

If the $I(\lambda, 2\theta)$ map obtained with a beam of large divergence is to be converted into $R(q_z)$ one assumes that all non-specularly reflected intensity can be neglected. Depending on the sample, the q_z range, and the dynamic range one measures, this might not be the case.

The specular intensity measured at a certain 2θ does not depend on the beam divergence (provided it is sufficiently large to illuminate the sample at an angle θ). The diffuse scattering for a given angle of incidence θ spreads over all 2θ so that the *incoherent background* for a certain 2θ is proportional to $\Delta\theta$. Off-specular scattering leads also to background, but with a different characteristics. Figure 10.4 illustrates this effect.

A consequence is that samples with a high contribution of incoherent background can not be measured with a wide divergence. Or more general, whenever crosstalk of the incoherent scattering attributed to θ into a

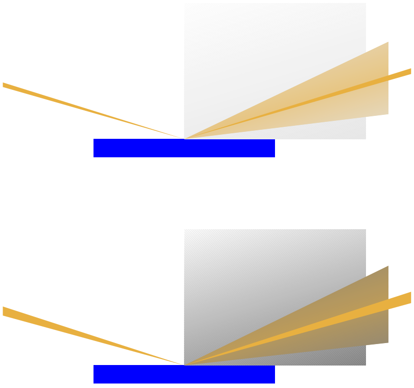

Figure 10.4: *Top*: A convergent beam with divergence $\Delta\theta$ impinging the surface under θ leads to specular scattering around 2θ with the same divergence. In addition a fan of off-specular scattering and a (non-flat) background from incoherent scattering is created. *Bottom*: A doubling of $\Delta\theta$ also doubles the total intensity of the specular contribution, but the incoherent background scales with 4 (2 times the incoming divergence and 2 times the detector angle). The off-specular contribution scales somewhere in between 2 and 4, depending on how fast it fades off away from the specular condition.

detection channel occurs, where specular scattering form an other θ is expected. This also holds for all kinds of multi-beam approaches.

The question is now, if one can use the *Selene*-type guide also for (almost) conventional measurements. We have performed test measurements with a liquid/solid sample cell, where the interface is illuminated through a thick Si-block of 100 mm length. Due to the insufficient quality of the reference measurement for normalisation, it is not possible to extract high-quality $R(q_z)$ curves from these measurements. But it is still possible to estimate the reduction of the incoherent background by using a slit behind the elliptic guide.

Figure 10.5: Maps of $\log_{10}[\,I(\lambda,\theta)\,]$ taken with the liquid/solid interface cell with Si vs. D_2O. *Left*: with a beam of $\Delta\theta = 1.1^\circ$ for 2 orientations $\omega = -0.7^\circ$ and $\omega = 0.3^\circ$. *Right*: The same geometries, but with a beam reduced to $\Delta\theta = 0.11^\circ$ by a diaphragm behind the guide.

Figure 10.5 shows $I(\lambda,\theta)$ maps for the cell filled with D_2O with a divergence of $\Delta\theta = 1.1^\circ$, and of $\Delta\theta = 0.11^\circ$, respectively. The incoherent scattering can be clearly seen for $\Delta\theta = 1.1^\circ$ in the range $\lambda \approx 3\ldots8$ Å, fading for longer λ. The reason for the fading is the width of the time-bin varying with λ. The bright triangle in the upper left map corresponds to the total reflection plateau, the streaks in the maps on the left are the specularly reflected beams. The maps for the low-divergent beam shows a strongly reduced background, which hardly affects the specular signal.

Bibliography

[1] D. Pantel, S. Goetze, D. Hesse, and M. Alexe. Reversible electrical switching of spin polarization in multiferroic tunnel junctions. *Nature Materials*, 11:289293, 2012.

[2] Phillip M. Bentley, Shane J. Kennedy, Ken H. Andersen, Damian Martin Rodriguez, and David F. R. Mildner. Correction of optical aberrations in elliptic neutron guides. *N.I.M. A*, 693:268–275, 2012.

[3] M. Russina, F. Mezei, and G. Kali. First Implementation of Novel Multiplexing Techniques for Advanced Instruments at Pulsed Neutron Sources. In *5TH EUROPEAN CONFERENCE ON NEUTRON SCATTERING*, volume 340 of *Journal of Physics Conference Series*, DIRAC HOUSE, TEMPLE BACK, BRISTOL BS1 6BE, ENGLAND, 2012. European Nucl Scattering Assoc, IOP PUBLISHING LTD. 5th European Conference on Neutron Scattering (ECNS), Prague, CZECH REPUBLIC, JUL 17-21, 2011.

[4] Maruyama R., Ebisawa T., Tasaki S., Hino M., Takeda M., Kawai T., Kawabata Y., and Sakai K. A resonance neutron-spin flipper for neutron spin echo at pulsed sources. *Physica B*, 335(1):238–242, 2003.

[5] J. Stahn. A switchable white-beam neutron polariser. *Physica B: Condensed Matter*, 345(1-4):243 – 245, 2004. Proceedings of the Conference on Polarised Neutron and Synchrotron X-rays for Magnetism.

[6] R. Cubitt. *N.I.M. A*, 558:547–550, 2006.

[7] R. Cubitt and J. Stahn. Neutron reflectometry by refractive encoding. *Eur. Phys. J. Plus*, 126:111, 2011.

[8] Frédéric Ott and Alain Menelle. Refocus: A new concept for a very high flux neutron reflectometer. *Nuclear Instruments and Methods in Physics Research A*, 586(1):23 – 30, 2008. Proceedings of the European Workshop on Neutron Optics - NOP '07.

[9] F. Ott and A. Menelle. New designs for high intensity specular neutron reflectometers. *European Physical Journal - Special Topics*, 167:93–99, 2009.

[10] M. Schneider, J. Stahn, and P. Böni. Focusing of cold neutrons: Performance of a laterally graded and parabolically bent multilayer. *Nuclear Instruments and Methods in Physics Research Section A: Accelerators, Spectrometers, Detectors and Associated Equipment*, 610(2):530 – 533, 2009.